Four-dimensional Variability of Composite Halokinetic Sequences

*Leonardo Muniz Pichel, Christopher A-L. Jackson

Basins Research Group (BRG), Department of Earth Science and Engineering, Imperial College London, South Kensington Campus, SW7 2BP, United Kingdom

*email: l.muniz-pereira@imperial.ac.uk

ABSTRACT

The architecture of salt diapir-flank strata (i.e. halokinetic sequences) is controlled by the interplay between volumetric diapiric flux and sediment accumulation rate. Halokinetic sequences consist of unconformity-bounded packages of thinned and folded strata formed by drape-folding around passive diapirs. These sequences are described by two end-members: (i) *hooks*, which are characterized by narrow zones of folding (<200 m) and high-angle truncations (>70°); and (ii) *wedges*, which are typified by broad zones of folding (300-1000 m) and low-angle truncations (<30°). Hooks and wedges stack to form tabular and tapered composite halokinetic sequences (CHS), respectively. CHSs were first and most thoroughly described from outcrop-based studies that, although able to capture their high-resolution facies variations, are limited in describing their 4D variability. This study integrates 3D seismic data from the SE Precaspian Basin, onshore Kazakhstan and structural restorations to examine variations in CHS architecture through time and space along diapirs with variable plan-form and cross-sectional geometries. The diapirs consist of curvilinear walls that vary from upright to inclined in cross-section, may flare-upward and locally display well-developed salt shoulders and/or laterally transition into salt rollers. CHS architecture is highly variable in both time and space, even along a single diapir or minibasin. A single CHS can transition along a salt wall and/or minibasin from tabular to tapered geometries. They can also be downturned and exhibit rollover geometries with thickening towards the diapir above salt shoulders. These variations can be linked to changes in the diapir morphology. Inclined walls present a greater proportion of tapered CHSs implying an overall greater ratio between sediment accumulation and salt-rise relatively to vertical walls. In terms of vertical stacking, CHS can present a typical zonation with lower tapered, intermediate tabular and upper tapered CHSs, but also unique patterns where the lower sequences are tabular and transition upward to tapered CHS. The study demonstrates that CHSs are more variable than previously thought, indicating a complex interplay between volumetric salt rise, diapir-flank geometry, sediment accumulation and roof dimensions. Ultimately, this improves our understanding of diapir-flank deformation and potential minibasin reservoir distribution.

1. INTRODUCTION

Salt diapirism and the associated development of minibasins are fundamental processes in salt-rich sedimentary basins. Salt diapirs can rise in response to extension (i.e. reactive diapirism), shortening (i.e. active diapirism), and differential sedimentary loading (i.e. passive diapirism) (Vendeville and Jackson, 1992; Hudec and Jackson, 2007). Passive diapirism is the syn-depositional growth of salt body at/near the free surface driven by a vertical load of sediments within surrounding minibasins; these sediments sink into the salt-source layer, thereby pumping salt into the diapir (Nelson, 1989; Jackson and Talbot, 1991; Rowan et al., 2003; Jackson and Hudec, 2017). This mechanism dominates the history of most and the largest diapirs known-to-date and ceases only when salt flow is outpaced by sedimentation, typically as a consequence of depletion of the source-layer (Rowan et al., 2003; Jackson and Hudec, 2017).

Passive diapirism is intrinsically linked to subsidence and deposition within flanking minibasins, deforming the minibasin and causing stratal thickness variations at two different scales: (i) minibasin-scale, which is associated with the development of broad, open folds that generally span the minibasin width; and (ii) diapir-flank-scale, which is associated with a much narrower zone of folding and stratal thinning, typically within 1 km of the salt-sediment interface (e.g. Vendeville and Jackson, 1991; Rowan et al., 2003; Giles and Rowan, 2012; Rowan et al., 2014). Syn-kinematic growth strata associated with diapir-flank scale deformation are referred to as halokinetic sequences (HS), which are defined as unconformity-bounded packages of thinned and folded strata adjacent to halokinetically-driven diapirs (Giles and Lawton, 2002; Giles and Rowan, 2012; Hearon et al., 2014). Deformation within these strata is controlled by drape folding and upturn of ephemeral, thin diapir-roofs and associated flank strata during passive diapirism. Rotation and flexure is accommodated by layer-parallel slip, with little to insignificant vertical (i.e. diapir-parallel) shearing or drag fold (Giles and Rowan, 2012; Rowan et al., 2003; 2014; Hearon et al., 2014; Jackson and Hudec, 2017).

Giles and Rowan (2012) define two halokinetic sequences end-members: i) *hooks*, characterized by narrow zones of folding (<200 m), high-angle truncations (>70°) beneath bounding unconformities, and abrupt facies transitions towards the salt-sediment interface; and (ii) *wedges*, which are typified by broad zones of folding (300-1000 m), low-angle truncations (<30°) beneath bounding unconformities, and gradual facies changes towards flanking salt (Fig. 1a). These are of parasequence scale (c. 10-50 m thick) and stack to form: i) tabular and ii) tapered composite halokinetic sequences (CHS), respectively (Fig. 1b), which are considered scale-equivalent to third-order depositional cycles (c. 100-1000 m thick) (Giles and Rowan, 2012). Tabular CHSs have a tabular form (parallel base and top boundaries), with axial-traces within each hook sequence being offset from each other and sub-parallel to the diapir margin (Fig. 1b). They are often associated with minor salt cusps that form where the unconformities intersect the diapir (Giles and Rowan, 2012) (Fig. 1b). Tapered CHSs have a tapered shape defined by converging upper and lower boundaries, with internal axial-traces that are inclined and curve away from the diapir margin (Fig. 1b).

These end-members are thought to be a function of the interplay between salt-rise rate (R), sediment accumulation rate (A) (Giles and Rowan, 2012) and, ultimately, roof thickness (Hearon et al., 2014). In cases where diapir rise-rate is greater than the sediment accumulation rate (R>A), hook halokinetic sequences will form, stacking to generate a tabular CHS. Conversely, wedge HS and tapered CHS sequences form when sediment accumulation rate outpaces diapir-rise rate (R<A). In the case where R>>A, the diapir will flare upward and eventually extrude an allochthonous salt sheet, whereas if R<<A, the diapir will narrow and eventually stop rising as it is buried. These sequences were first and most thoroughly described from essentially two-dimensional, outcrop-based studies (cf. Giles and Lawton, 2002; Giles and Rowan, 2012; Saura et al., 2014; Kergaravat et al., 2016; Martín-Martín et al., 2017; Moragas et al., 2018) that, although able to capture their high-resolution facies variations, are limited in terms of what they reveal about the four-dimensional variability of such salt-sediment interactions. Hearon et al. (2014) is the only study so far describing the

style and geometry of CHSs using seismic data from the northern Gulf of Mexico. Although they provide important insights into the 3D architecture and temporal variations in CHSs, they are limited in that they explore only a single, geometrically rather simple, plug-like diapir (i.e. stock) defined by an essentially vertical salt-sediment interface.

We here use 3D time- and depth-migrated seismic data from the SE Precaspian Basin, onshore Kazakhstan to examine vertical and lateral variability in CHS architecture along diapirs (stocks and walls) with variable planform and cross-sectional geometries. We adopt a similar approach to Hearon et al. (2014), integrating seismic data and structural restorations to analyse variations of CHS architecture at present-day and at the time of their formation. We also use our restorations to demonstrate, for the first time, the sequential evolution of the diapirs and associated CHS strata. We focus on answering the following questions: 1) How laterally variable are CHSs along salt walls and in thick minibasin successions? 2) What is the relationship between CHS architecture and different cross-sectional diapir geometries (i.e. inclined, upright and salt shoulders)? 3) What controls these variations? 4) How diapir-flank and minibasin-scale deformation are related? And 5) What implications does CHS variability have for diapir-flank hydrocarbon-reservoir pinch-out?

2. GEOLOGICAL FRAMEWORK

The Precaspian Basin is a large (540,000km^2), elliptical basin located at the northern edge of the Caspian Sea in Kazakhstan and Russia, on the SE edge of the East European Craton, near the present southern margin of Eurasia. The basin initially formed in response to Devonian rifting and subsequent Carboniferous, post-rift thermal subsidence (Barde et al., 2002a,b; Volozh et al., 2003). The Ural Orogeny started in the middle Carboniferous in response to the collision of the eastern European and Kazakh plates, causing uplift of the Precaspian Basin's eastern side and the development of a rapidly-subsiding foreland basin in the remaining Precaspian Basin until the Lower Permian (Brunet et al., 1999; Barde et al., 2002b). During this time (i.e. Kungurian-Kazanian) the basin became isolated from the Tethys

Ocean and a thick (up to 4.5 km in the basin; c. 2 km in the study-area) salt sequence was deposited (Barde et al., 2002b, Volozh et al., 2003; Fernandez et al., 2017). During the Upper Permian, sedimentation was dominated by siliciclastic progradation from material shed off the rising Ural Mountains, loading and expelling salt up into rising diapirs and and basinward towards the west (Volozh et al., 2003). This resulted in development of broadly margin-parallel, N-oriented salt walls and expulsion rollovers near the eastern basin margin (Duffy et al., 2017; Jackson et al., 2019).

Farther west and within our study-area, the salt-related structural framework is characterized by a polygonal pattern of salt walls and sub-circular minibasins, with individual walls being up to 20 km long, 8 km wide and with up to 5.5 km of vertical relief (Duffy et al., 2017; Fernandez et al., 2017). A series of up to 1 km thick minibasins, containing evaporites and non-marine clastics, formed in the Late Permian, subsiding into and now being fully or partially encased in Lower-Middle Permian salt (Fig. 2c). A subsequent generation of (supra-salt) minibasins formed by load-driven subsidence and passive diapirism during the remaining Late Permian to Triassic (Duffy et al., 2017; Jackson et al., 2019). These minibasins are up to 10 km in diameter and up to 5.5 km deep, being typically welded to the pre-salt interval and/or to the encased minibasins (Duffy et al., 2017; Jackson et al., 2019). Jackson et al. (2019) show that these minibasins are characterized by lower bowl- and upper wedge-shaped units, which record periods of symmetric and asymmetric subsidence, respectively, the cause for which is unclear. Our study focusses on the geometry, stratigraphic architecture and deformation styles of diapir-flank strata within these minibasins and their associated salt-sediment interface, which may, ultimately, help understanding the controls in the variables styles of subsidence and diapirism in the area.

The minibasins are capped by the Base Jurassic Unconformity (BJU) recording a major erosional event associated with the Late Triassic Cimmerian Orogeny (Volozh et al., 2003). Minibasins and diapirs are overlain by a gently-folded Jurassic-Lower Cretaceous section associated with a series of regional, Late Cretaceous-Miocene shortening events related to

the collision of Arabia and India with Asia (Volozh et al., 2003; Duffy et al., 2017). These pulses of shortening were relatively mild in the area due to its distance to the collision front, being mostly accommodated by squeezing of diapirs between laterally mobile, albeit stronger and relatively undeformed supra-salt minibasins (Duffy et al., 2017; Jackson et al., 2019).

3. METHODS AND DATASET

3.1. Seismic Interpretation

We use a time-migrated 3D seismic reflection dataset that together covers 2532 km^2 of the eastern Precaspian Basin (Fig. 2), imaging up to 6 seconds of two-way time (TWT), and with a vertical sample rate of 2 milliseconds (ms) and inline (E-W) and crossline (N-S) spacing of 20 m. The seismic data is presented with Society of Economic Geologists (SEG) 'normal polarity', where a downward increase in acoustic impedance is represented by a positive reflection event (white on seismic sections) and a downward decrease in acoustic impedance is represented by a negative reflection event (black on seismic sections). Our time-migrated data has better imaging of supra-salt minibasin stratigraphy than the depth-migrated volume used by Duffy et al. (2017) and Fernandez et al. (2017) to analyse the more deeply buried encased minibasins. We therefore conduct the detailed analysis of seismic-stratigraphic patterns within minibasins and halokinetic sequences on the time-migrated data, using a seismic velocity volume to perform depth-conversion of key sections. Due to its better imaging of more deeply buried structures, we use the depth-migrated data to constrain the large-scale morphology of diapirs and minibasins (e.g. top-salt depth map, fig. 3), and to test the accuracy of our depth-converted sections.

Various boreholes lie within the study-area, although most are relatively shallow, terminating in Upper Triassic strata. Some wells do penetrated to deeper depths, although they were targeting encased minibasins and, therefore, penetrate areas of thick-salt (i.e. diapirs) and do not intersect the intervening supra-salt basins (see Duffy et al., 2017; Fernandez et al., 2017).

For this reason, we have limited age control of the supra-salt minibasin strata. However, given the Lower-Middle Permian age of the salt, and the stratigraphic position of the distinct Base Jurassic Unconformity (BJU), the minibasins are likely of Late Permian-Triassic age (see above). Despite the lack of borehole data, we utilize seismic stratigraphic relationships and geometries to map and define unconformity-bounded packages (i.e. CHS) near the diapir flanks. We present on CHSs within three seismically well-imaged minibasins that; i.e. because of the good to excellent image quality, we can confidently map the geometry of the salt-sediment interface and the diapir-flank stratal architecture. These minibasins are also flanked by diapirs with distinct cross-sectional styles and planform geometries, allowing us to analyse the 4D variability of CHSs over a range of different diapir geometries and styles (i.e. upright vs. inclined salt walls, salt walls vs. stocks and salt shoulders). We mapped a series of 16-18 CHS within each minibasin using a 200 x 200 m grid, in addition to mapping base- and top-salt, and the Base-Jurassic Unconformity (BJU).

3.2. Depth-Conversion and Structural Restoration

The main criteria used to distinguish different types of seismically imaged CHS are the geometry and width of folding/stratal thinning (cf. Hearon et al., 2014). Given that these are both broadly sub-horizontal parameters, vertical exaggeration in our time-migrated data do not greatly affect any extracted values. However, to more accurately quantify the CHS geometries, we perform depth-conversion for each example presented here, using the seismic velocity volume mentioned above. Additionally, we perform 2D structural restorations using 2DMove© to compare and quantify parameters such as tapering angles and folding zone width for both present and original CHS geometries, thereby eliminating distortions caused by post-depositional deformation, burial and compaction (tables 1-3). The restoration approach and quantitative analysis are based on the method defined by Hearon et al. (2014), and utilizes the decompaction and flexural-slip unfolding algorithms (see Rowan et al., 2003; Rowan and Ratliff, 2012 for salt restoration algorithms). Vertical decompaction was conducted based on

158 the Sclater and Christie (1980) compaction function for sand and shale, which is appropriate
159 given the known composition of the suprasalt minibasins.

160 4. COMPOSITE HALOKINETIC SEQUENCE VARIABILITY

161 Suprasalt minibasins formed during the Upper-Permian Triassic in response to differential
162 loading and passive diapirism (see Jackson et al., 2019). In many of them, CHSs are not
163 visible due to: i) minibasin tilting and associated rotation of near-flank strata to near-vertical
164 due to late-stage shortening and diapir squeezing (Duffy et al., 2017) and/or ii) the presence
165 of large salt overhangs, which make imaging of the sub-diapir flank strata difficult. We thus
166 focus our analysis of CHS geometry on two distinctly different diapir geometries observed
167 around three minibasins: 1) an inclined-diapir margin (Fig. 4a), and 2) a vertical salt wall that
168 passes along-strike into a salt roller (Fig. 4b). We first describe how the CHSs vary vertically
169 in individual cross-sections and, then, laterally by comparing multiple cross-sections and 3D
170 images.

171 In all examples, the CHS are bounded by pronounced erosional unconformities that extend <
172 1 km away from the diapir margin, passing into correlative unconformities towards the
173 minibasin centre (Fig. 4). The CHS are upturned and in direct contact against the diapir, and
174 have variable degree of folding, thinning and structural relief (Fig. 4, tables 1-3). Where the
175 salt-sediment interface dips gently and the diapir-flank seismic imaging is best, we observe
176 minor salt cusps where bounding unconformities intersect the diapir; these are especially
177 prominent in tabular CHS (Fig. 4a). In general, the CHS present multiple internal
178 unconformities associated with higher-order halokinetic sequences (cf. Giles and Rowan,
179 2012) and present basal onlaps at or near their axial-traces (Fig. 4). In other cases, especially
180 within tabular CHS, low-continuity-to-chaotic facies appear to interfinger with more continuous,
181 brighter reflections near the diapir-margin, possibly indicating debris flows sourced by material
182 eroded from the diapir's crest (Fig. 4).

183 4.1. Inclined Diapir

4.1.1. Overall geometry

In our first example, we analyse the CHS architecture on the southwest flank of a semi-circular minibasin associated with a c. 12 km long curvilinear salt wall that has an inclined flank (40° in its lower section increasing to 60° in its upper section; Figs. 5-7). The minibasin tilts to the SW due to shortening-induced uplift of its NE flank; in contrast, the southwest wall and associated CHS strata, which form the focus of our analysis, remain essentially undeformed. This tilting made the dip of the southwest salt wall even gentler, allowing higher resolution and confidence in the definition of the salt-sediment boundary and CHS stratigraphic architecture than in previous studies focused on very steep-sided salt diapirs (Fig. 4a) (cf. Hearon et al., 2014).

4.1.2. Minibasin and CHS architecture

The first stage of diapir growth was controlled by minibasin-scale subsidence as evidenced by a lower bowl-shaped stratigraphic section with a sub-vertical synclinal axial-trace at its centre (Figs. 5-6) (cf. Rowan and Weimer, 1998; Jackson et al., 2019). The second stage was characterized by a switch in the location of depocentres towards the flank of the diapir as indicated by the large-scale wedge geometry associated with at least 16 CHS observed in profiles sub-parallel to the wedge dip-direction (Figs. 5-6). The inclined wall is flanked largely by tapered CHS (Figs. 5-6), with only one (northern section, fig. 5) and two CHS (central section, fig. 6) out of the 16 being classified as tabular (table 1).

In general, tabular CHS are relatively thinner (150-250 m at present, fig. 8 and 180-300 m decompacted, fig. 9) than tapered CHSs (150-450 m at present, fig. 8 and 180-520 m decompacted, fig. 9) and occur towards the intermediate-to-late stages of diapir rise and minibasin subsidence (i.e. in the middle and uppermost parts of the minibasin; CHSs 13-14, fig. 5 and CHS 13, fig. 6). Tabular CHS have folding and thinning zones ranging from 90-185 m of width (100-200 m restored) and tapering angles of 60-64° (54-60° restored, Table 1), values that are relatively low when compared to tabular CHS associated with the upright wall

(see section 4.2.). The tapered CHS have a folding and thinning zone ranging from 360-940m (420-1000 m restored) and tapering angles of 8-44° (12-35° restored).

The minibasin and individual CHS become, in general, thinner to the south, with this being associated with a switch from dominantly tapered (Figs. 5-6), to a mixture of tabular and tapered CHSs (Fig. 7, table 1). CHS end-member distribution is also notably different in the south, with tabular CHS occurring in the lower and uppermost sections, and being separated by an intermediate section with tapered CHS (Fig. 7). The lower CHSs (1-6), which have typical tapered geometries in the northern and centrals sections (Figs. 5-6), have, in the south, a narrow (< 100 m) zone of folding and thinning towards the diapir, with prominent salt cusps intercepting their unconformities (Fig. 7, table 1), a geometry typical of tabular CHSs (cf. Giles and Rowan, 2012; Hearon et al. 2014). These CHS also become condensed to the south, being only c. 80-100 m thick (fig. 7), which is equivalent to the thicknesses of higher-order, halokinetic sequences (Giles and Rowan, 2012). CHS 14-16, despite maintaining their thickness, also switch from tapered to tabular geometries to the south (Fig. 5-7, table 1).

The lowermost CHSs (1-4, table 1) present more unique lateral variations, demonstrating increasing influence of larger, minibasin-scale folding and subsidence towards the centre of the salt wall (Figs. 5-6). Although, their geometries are indicative of diapir-margin processes, i.e. their thinning and folding still occurs near the diapir margin, the width of folding zone increases up to 2100 m away from the diapir and tapering angles are considerably lower (11-14° restored, table 1, fig. 8).

4.1.3. Diapir and Minibasin Evolution

The preponderance of tapered CHSs in the inclined diapir example suggests that the development of gently-inclined salt walls is associated with a dominant higher sediment accumulation rate (A) relative to the net salt-rise rate (R) and/or volumetric salt flux (q) (cf. Jackson and Hudec, 2017) (Figs. 5-6 and 8-9). This is supported by the fact that the wall exhibits a subtle steepening of its margin through time (from c. 40 to 60°) that correlates with

a general upward narrowing of the zone of folding and thinning of minibasin strata (Table 1 and fig. 9), which, in turn, implies a relative increase of R/A or q/A.

In addition, the CHS geometries and distribution are also variable along-strike as shown by the greater proportion of tabular CHS geometries to the south (Fig. 7), where the salt wall is also steeper (Figs. 5-7). This southward transition from tapered to tabular CHS geometries may be associated with: i) significant thinning of individual CHS (e.g. CHS 1-5) and, thus, a lateral decrease in the sediment accumulation rate to a point lower than the salt-rise rate; or ii) variable diapir-rise rate in cases where CHS thickness does not vary along-strike (e.g. CHS 14-16). The latter may thus be better explained by volumetric (i.e. 3D) salt flux variations and local variations of roof thickness and width, rather than the classical two-dimensional A/R ratios (cf. Giles and Rowan, 2012) (see discussion).

4.2. Vertical salt wall

4.2.1. Overall Geometry

Our second example comes from two adjacent minibasins flanking a 3-4 km tall, 3 km long and 1-2 km wide N-oriented salt wall that protrudes northwards out of a much larger (> 20 km long), W-oriented wall (Fig. 3). The diapir is upright, and has a sub-vertical upper flank and a more gently-dipping lower flank (Fig. 10). It varies in shape and dimension along-strike, passing northwards into a smaller diapir containing a 1.5 km wide salt shoulder (*sensu* Giles et al. 2018) half-way up its western flank (Fig. 11); and ultimately into a salt roller (sensu Vendeville and Jackson, 1992a) at its northernmost end (Fig. 12). Because the two minibasins are connected around the diapir and roller at their northern end, it is possible to constrain the relative ages of CHSs on each side of the diapir (Figs. 4-6.). This provides a unique opportunity to analyse how: i) a single CHS can vary across a salt wall with laterally variable cross-sectional geometry, ii) how two minibasins associated with the same salt wall can have variable CHS architecture, and iii) how CHSs transition from halokinetically-driven diapirs (passive and/or active) to diapirs driven by extension (i.e. reactive).

4.2.2. Minibasin and CHS architecture

The diapir is flanked on both sides by CHS (Figs. 10-11). Both minibasins contain a lower, 1-1.5 km thick, bowl-shaped section, which is c. 400 m thicker in the western minibasin than in the eastern minibasin (Fig. 10). This section thins northwards, towards the edge of the salt diapir, with age-equivalent strata showing typical CHS geometries (i.e. narrow zones of folding and thinning). The overlying stratigraphic succession is composed of strata with localized (< 1 km) thinning and folding near the salt-sediment interface characteristic of CHSs (tapered and tabular), and a broadly constant thickness (on average 90-320 m thick at present-day) towards the minibasin centre (Figs. 10-11).

There are drastic variations in the geometry and distribution of CHSs between the two partially-connected minibasins (Figs. 10-11). In Section 1, the western minibasin is dominated by tapered CHSs from the earliest-to-intermediate (CHSs 1-12) and final stages of diapir growth (CHSs 17-18) with four non-tabular (e.g. tapered and transitional) CHSs in the intermediate-upper section (CHSs 13-16, fig. 10, table 2). The tapered CHSs are characterized by thinning and folding zones ranging from 370-1970 m (350-1180 m restored) with an average of 830 m (720 m restored), and taper angles of 13-49° (11-30° restored) with an average of 31° (18° restored) (Table 2). The tabular CHSs have folding zones ranging from 45-190 m (30-155 m restored) with an average of 100 m (present-day and restored) and taper angles of 52-74° (50-72° restored) with an average of 64° (60° restored) (Table 2). Conversely, the eastern minibasin is dominated by tabular rather than tapered CHSs, with only two tapered (CHS 2 and 10) and two transitional CHSs (CHS 1 and 5). The two tapered CHS have thinning and folding zones ranging from 300-810 m (310-915 m restored) and tapering angles of 18-26° (17-18° restored) (Table 2). The tabular CHS have folding zones varying from 45-190 m (45-170 m restored) with an average of 96 m (109 m restored), and with taper angles of 40-71° (36-68° restored) with an average of 57° (52° restored) (table 2).

Only CHSs 2, 10 and 14-16 have the same end-member geometries across the diapir and even when classified as the same end-member, each of them differ across the diapir in terms of the width and degree of tapering (Table 2). Their thickness also varies, with CHSs being generally thicker on the western, tapered CHS-dominated minibasin (Figs. 10 and 13a). The largest thicknesses contrasts occur within CHSs 3-7, which are tapered and up to 320 m thick on the west minibasin, and tabular and only 90-150 m thick in the east minibasin (Fig. 13a). This CHS variability can be linked to changes in the diapir morphology on both of its flanks (Fig. 4). The lower-to-intermediate diapir section (between CHSs 1-5) presents a subtler, gently-dipping (c. 40-50°) flank with a series of narrow (c. 300-500 m), sub-horizontal (15-30°) salt shoulders on the west where tapered CHSs predominate (Fig. 10). Conversely, the equivalent, lower-to-intermediate eastern diapir flank is steeper (55-65°), has no recognizable salt shoulder and is largely associated with tabular CHSs (Fig. 10). The upper diapir flanks are sub-vertical (c. 90°) on both sides and predominantly associated with tabular CHSs (CHSs 13-16) on both minibasins, although the final two (CHS 17-18) present tapered and tabular geometries on the west and east minibasin section, respectively (Fig. 4).

Section 2, another dip-oriented section located 1.2 km further north of Section A, demonstrates how CHS and diapir geometries vary significantly over a relatively short along-strike distance (Fig. 11, table 3). In this location the salt wall is shorter (c. 2.8 km tall) and present a broader (1.5 km wide), clearly-defined salt shoulder relative to the previous section (Fig. 10). Strata age-equivalent to CHSs 13-18 from Section A (Fig. 10) are not classified as CHS, as they cover the diapir and show no diapir-related thickness variations (Fig. 11). The tabular CHSs, all in the western minibasin, have present folding zones varying from 20-200 m (average of 93 m) and tapering angles from 42-86° (average of 65°) (Fig. 11, table 3). The tapered CHSs have a folding zone with 325-1100 m of width (average of 480 m) and 11-49° of tapering (average of 30°) (Fig. 11, table 3).

The eastern minibasin in Section 2 shows a similar distribution of CHSs to that seen in Section A (Fig. 10), but with a greater proportion of tabular geometries (i.e. all but the last CHS are

tabular; Fig. 11, table 3). The western minibasin, however, exhibits more marked along-strike variations; it has no tabular CHSs and contains CHSs (2-5) that are downturned and thickened (30-55 m of thickening, figs. 11 and 13b) towards the diapir. All other CHSs (1 and 6-12) are tapered. Sequences 2-5 are therefore not, by definition, CHS, as this requires diapir-flank upturning and thinning, *sensu stricto* (see Giles and Rowan, 2012). They are, nonetheless associated with classic tapered CHS geometries 1 km further south and are driven by diapir-flank deformation, i.e. thickness variations and folding occur within 370-680 m from the salt-sediment interface, but with different kinematics. Their rollover geometry and location over an area of pronounced narrowing of the diapir (i.e. salt shoulder) suggest that they formed due to salt expulsion and/or dissolution-related collapse (cf. Giles et al., 2018). We test these hypotheses in the discussion (section 5.2.).

Another 1.2 km further north (Section 3), the structure changes completely from a diapir to a salt roller nucleating onto gently inflated salt (Figs.10-12). The upper salt roller is defined by an east-dipping listric normal fault on its eastern flank that is overlain by a west-verging, extensionally faulted, extensional rollover. This structure is notably different from the ones seen further south such that their age-equivalent strata do not present typical CHS geometries (i.e. diapir flank upturning and thinning). Sequences 1-10 are all downturned towards the roller on both of its sides and present typical hangingwall thickening on the eastern side (Fig. 12). Strata are broadly isopachous on the footwall, although subtle thinning occurs between sequences 1-3, which onlap the earlier diapir and, thus, may be classified as tapered CHS that were later collapsed and downturned due to extension (Fig. 12).

The unique along-strike variations in CHS architecture and diapir morphology described above are better visualized in 3D (Fig. 14). A 3D image shows how a single CHS transitions from: i) a tabular geometry with abrupt thinning towards the diapir eastern flank to, ii) localized downturn above a salt shoulder to the northwest, and to, iii) a tapered geometry that extends 350 m upward along the western diapir flank (Fig. 14). Northwards, towards the axis of the larger depocentre, the CHS gives way to fault-related hangingwall thickening over a salt roller

until it switches again to typical CHS geometries associated with a different salt wall further north (Fig. 14).

4.2.3. Diapir and Minibasin Evolution

Sequential structural restorations illustrate the evolution of the salt wall and associated growth strata, helping explain the observed CHS variability along the two, partially-connected minibasins (Figs. 15 and 16, supplementary material). The restoration demonstrates that the diapir grew passively and asymmetrically since its earlier stages, with a gentler western flank and steeper eastern flank (Figs. 15-16). This correlates directly with the development of tapered CHSs on the gently-dipping side and tabular CHS on the steeply-dipping side. Moreover, the restorations also show that the coeval development of different CHS end-members on each side of the diapir is associated with how far syn-kinematic strata extends across the diapir flank and/or onto its crest (Fig. 15). The CHS are, therefore, formed as temporary roofs that are shouldered aside and upturned due to continuous salt rise (cf. Rowan et al., 2003) but that, in these cases, never completely cover the diapir (Fig. 15).

The restorations also show how the development of tapered geometries that extend 200-350 m along the western flank of the diapir (CHSs 1-9) is related to the occurrence of salt shoulders. These narrow shoulders are partially destroyed due to continuous salt rise, which also reduces the diapir asymmetry and overall width, and produces additional rotation of previously-formed CHSs (Fig. 15). Some of these early tapered CHSs (CHSs 2-4, fig. 15) formed small-scale anticline-syncline pairs along the flank of the diapir as they onlapped supra-shoulder strata and/or the shoulder itself. These units may indicate a brief episode of minor shoulder-collapse by dissolution (cf. Giles et al., 2018). The width of the salt shoulders varied along-strike (Figs. 15 and 16). Where it formed a km-scale feature, supra shoulder strata collapsed above it, forming a rollover with localized, minor thickening towards the diapir (CHSs 2-5, fig. 16).

5. DISCUSSION

5.1. How laterally and vertically variable are Composite Halokinetic Sequences?

Our study confirms the hypothesis of Hearon et al. (2014) that different CHS end-members can form along the same diapir at the same time. However, we demonstrate that CHSs can vary even more drastically and frequently across salt diapirs than previously described. All CHSs analysed in this study have laterally variable width of drape folding, tapering angles and relief (Figs. 5-7, 10-11 and Tables 1-3) and stratal terminations. This corresponds to an overall greater lateral variability than observed in Hearon et al. (2014), where only three CHSs (less than 10% of the total number analysed) varied along-strike. These variations can be relatively subtle so that the CHS end-member is not altered but, in many cases, CHSs can vary from one end-member to another within the same minibasin and over only <1 km along strike (Figs. 5-7 and 10-11, tables 1-3). Additionally, a single CHS can vary between tabular and tapered end-member geometries along-strike and across the same diapir and within two different, albeit partially-connected minibasins (Figs. 10-11, tables 2-3). CHS relief can also change significantly (c. 100-300 m) along an individual CHS, especially in the case of tapered end-members that can reach up to 400 m of structural relief (cf. CHSs 5 and 7-11, figs. 6; CHSs 4, 6 and 8, fig. 10).

These sequences can also transition *laterally* from CHS (i.e. locally upturned and thinned) into non-CHS strata. They can, for example, transition in only ~1 km along-strike into downturned, folded and thickened strata (i.e. rollovers, fig. 11). They can also switch laterally into normal-fault-driven thickened strata overlying salt rollers, or even into isopachous and relative undeformed strata away from the larger, halokinetically-driven structure, in which case they are not even classified as CHSs (Figs. 11-12). These sequences can also transition along-strike from being controlled by diapir-flank scale deformation, to being influenced and even driven by minibasin-scale subsidence towards their centre (cf. Rowan et al., 2016), which typically occurs within deeper and older CHSs (Figs. 5-6 and table 1, see section 5.4).

The classic CHS succession *vertical* zonation consists of lower tapered, intermediate tabular and upper tapered CHSs (Giles and Rowan, 2012; Hearon et al., 2014). The transition from lower tapered CHSs to tabular CHSs is associated with an increase of salt-rise rate as the minibasin gradually thickens, gets denser, and continues to pump salt into the flanking diapirs. As a continuum of this process, the source-layer is gradually depleted, resulting in a decrease in the salt-rise rate and, as a consequence, a switch from tabular to tapered CHSs (Giles and Rowan, 2012). Our work shows that switches from tabular to tapered end-members can be more frequent than previously thought (Table 2). These switches are commonly associated with marked changes in diapir shape such as salt shoulders (Figs. 10-11 and 15-16) (see section 5.2). Moreover, the CHS succession can also display different vertical patterns other than the classical two-part vertical zonation (Figs. 7 and 10-11, tables 1-3). For example, the vertical wall shows an eastern minibasin with dominantly tabular CHS throughout its stratigraphic succession, including the lower and upper sequences, and only one tapered (CHS 10) and one transitional CHS (5) within its intermediate section (Fig. 10, table 3). The adjacent minibasin shows the opposite, with the classic tapered-tabular-tapered vertical zonation (Fig. 10, table 3). The inclined wall displays a more typical zonation along most of its length, having a dominantly tapered CHS succession with only a few tabular CHSs within its intermediate-upper stratigraphic section. This is however, completely different towards its southern portion where the lower and uppermost sections are composed of tabular CHSs with intermediate tapered CHSs (Fig. 7, table 1).

5.2. What is the interplay between different diapir cross-sectional geometries and CHS architecture?

5.2.1. Geometrical variations between different diapirs

This study provides the first-ever analysis of CHS architecture across different types of diapirs, i.e. with vertical (section 4.1) and inclined (section 4.2) cross-sectional geometries. Vertical diapirs demonstrate a greater proportion of tabular CHSs (27% on west minibasin to 78% on

east minibasin) relative to inclined diapirs (8-50%). This suggests that, for vertical diapirs and at a CHS time-scale, the diapir-rise rate is generally greater through time than the sediment accumulation rate when compared to inclined diapirs. This example also shows that even broadly symmetric diapirs can have highly-asymmetric adjacent minibasins. Same-age strata on both sides of the diapir display, in most cases, contrasting end-member CHS geometries and up to 100 m of thickness variations (Figs. 10-11, 13 and tables 2-3). This suggests asymmetric minibasin subsidence and, thus, salt expulsion and diapir rise (Figs. 15-16), characteristics that can be related to a regionally, three-dimensionally complex pattern of salt flow and minibasins subsidence as described by Jackson et al. (2019) and shown in numerical models of Fernandez et al. (2019).

The inclined wall shows that, in addition to the general greater proportion of tapered CHSs, the ratio of tapered CHS is higher towards their centre (Figs. 5-7 and table 1).There is commonly an increase in the width of the folding/thinning zone, and a decrease of tapering angles of tapered CHSs, towards the centre of the wall (CHSs 7-16, table 1), although there can also be an increase towards the north in a few cases (compare CHSs 17-19, table 1). Ultimately, this demonstrates laterally variable diapir-rise and minibasin subsidence through time (cf. Jackson et al., 2019; Fernandez et al., 2019). The gently-dipping diapir margin and the architecture of the flank strata suggest that in the case of inclined walls, sediment accumulation-rate tends to be greater than diapir-rise rate, which is the opposite to that inferred for vertical walls. As salt diapirs typically grow vertically when salt-flow rates equal sediment aggradation rates (Vendeville and Jackson, 1991; McGuiness and Hossack, 1993), the sedimentation rate is expected to be slightly higher than salt-rise rate at CHS time-scale for inclined diapirs. Nonetheless, at a larger, minibasin-time-scale, salt flow can still keep up with sedimentation as evidenced by continuous salt rise. The inclined walls also demonstrate relatively longer and greater influence of early-stage minibasin-scale subsidence and deformation as indicated by up to 2.5 km thick bowl-shaped lower sequence (Fig. 6) relative to a c. 200-500 m thick equivalent sequence associated with the vertical wall (Figs. 10-11).

5.2.2. Salt Shoulders

Salt shoulders are zones of abrupt diapir narrowing due to differential salt-rise from the diapir margin to its centre as a function of salt supply, dissolution and roof thickness (Giles et al., 2018). Salt shoulders are recognized in our study-area and present variable stratal architecture and transition patterns between non-shoulder and shoulder-related strata. They can be characterized by: i) a switch from tabular CHS to tapered CHS, ii) a marked increase in the width of folding and thinning of tapered CHSs, and iii) rollovers or downturned strata.

The simpler scenario is the abrupt change between tabular and tapered CHS end-members occurs over a narrowing salt-sediment interface (Fig. 17, CHS 3-4). In this case, there is a drastic increase in the width of folding, from c. 100 m below to 650 m above the shoulder and over the erosional unconformity defining the top of a series of tabular CHSs (Fig. 17). In the second case, similar increases in the width of the folding and thinning zone occur without changes to a different CHS end-member. This is visualized in the western flank of the vertical wall by pronounced lengthening (in the order of 170-300 m) of the zone of folding between tapered CHSs 4 and 5, 5 and 6, and 6 and 7 (Figs. 10 and 15, table 2).

The third shoulder scenario presents a more complex and remarkable supra-shoulder stratal architecture. In this case, pre-shoulder CHSs transition upwards over the shoulder into downturned and folded sequences that thicken towards the diapir with a characteristic rollover geometry (CHSs 2-5, Fig. 11). Their geometries may suggest: i) salt expulsion from the shoulder towards the central part of the diapir, ii) an extension-driven faulted-contact, or iii) shoulder collapse due to dissolution (Giles et al., 2018). As salt expulsion and associated rollover geometries are typically associated with leaning salt walls (Schuster 1995; Ge et al., 1997; Jackson et al. 2015b; Pichel et al., 2019a), and the wall presented here is broadly vertical, we reject the hypothesis of an expulsion-driven origin. Given that the zone of thickening is localized (c. 1.2 km long) and that equivalent strata in the adjacent minibasin are CHSs, implying halokinetically-driven diapirism, we also reject the extension-driven

hypothesis. Based on our structural restoration (Fig. 16) and the fact that shoulders may be related to higher rates of salt flank dissolution (Giles et al. 2018), we interpret that this rollover formed due to dissolution-related collapse.

5.3. What controls CHS variations?

Previous studies have described the development of different CHS end-members as a function of the relative rates of salt-rise (R) and sediment accumulation (A) (Giles and Rowan, 2012). A more recent study by the same authors defined that, although influenced by relative rates of salt rise and sedimentation, CHSs are primarily controlled by diapir-roof thickness (Hearon et al., 2014). We concur with these hypotheses but we add that diapir rise and sediment accumulation rates can vary along and across the diapir, generating spatial variations in roof thickness along the length and width of the diapir. This is, ultimately, driven by three-dimensionally variable diapir-rise (i.e. volumetric flux), something not depicted in previous CHS models (Fig. 18).

Variable sediment accumulation and volumetric salt flux, and consequently minibasin subsidence generates thickness variations within individual CHSs as observed in our examples (Figs. 5-8, 10-13). These variations may be a function of the direction of sediment input into the minibasin, differential erosion and/or subsidence around the diapir. Although the sediment input direction seems to have an influence in the two partially-connected minibasins, as suggested by CHSs with highly variable thicknesses (Fig. 13) around the salt wall, this is not clear for each of their CHSs, nor for the inclined wall. Regardless of the cause, individual CHS can change in thickness by up to 100% between the partially-connected minibasins (see restored CHSs 4 and 7, fig. 13). As a consequence, the CHS end-member varies for same-age strata across the diapir in the large majority of CHSs, with thicker tapered geometries on one side and thinner tabular geometries on the other (Figs. 10-11 and tables 2-3). This is expected given that tapered CHSs are typically associated with relatively higher sediment accumulation rates than tabular CHSs (Giles and Rowan, 2012). Overall minibasin thickness

and subsidence are logically also greater where CHS are dominantly tapered and thicker, i.e. western minibasin (Figs. 10-11).

CHS architecture also varies regardless of sediment thickness (e.g. CHSs 8-9 and 11, with equal thickness and different end-member geometries, fig. 13), which indicates an additional control to sediment accumulation. We argue that the localized thickness variations characteristic of CHS growth strata are controlled by how further inboard they extend above the diapirs. This is fundamentally governed by the three-dimensionally variable salt flux (q) within the diapir. Tapered CHSs form when sediments extend 300-1000 m over the diapir flank towards its crest, whereas tabular CHS typically extend over 50-200 m over its flank (Figs. 9 and 15-16). This is seen in our restorations where CHSs of broadly equal thickness across the diapir are characterized by distinct tapering angles and width of drape-folding, principally as a consequence of how far they extend across the diapir crest (Fig. 15). As a consequence, tapered CHSs results in gentler and wider diapir margins than tabular CHSs that are associated with more abrupt, steeper interfaces. Progressive diapir rise, nonetheless, displaces and rotates the CHS salt-sediment interfaces from an initially crestal position to the sides of the diapir, partially masking their original shape (Figs. 9, 15 and 16).

Restorations also demonstrate that tapered CHS can occur over transient salt shoulders that record a period of diapir narrowing. We note that this may occur on only one flank of the diapir (Fig. 15). Tapered CHS that extend for > 200 m along the present-day flank of the diapir (Figs. 6, 9, 10 and 11) were originally formed over transient salt shoulders. These salt shoulders may be preserved depending on the degree of subsequent diapirism and differential diapir-rise. We thus suggest that, in addition to i) diapir-flank dissolution-collapse, ii) greater roof erosion at the diapir centre and iii) fault-related weakening of the central roof (cf. Giles et al., 2018), salt shoulders can also develop due to: iv) roof thickness variations associated with tapered CHSs that extend further inboard over the diapir.

5.4. How CHSs interact with minibasin-scale subsidence?

At early stages of diapir rise and minibasin formation, subsidence is dominantly accommodated by broad, multi-km-scale synclinal folding, stratal thinning and onlap towards the diapir (i.e. bowl-shaped minibasins, Figs. 5-6 and 10). In later stages, subsidence tends to be more evenly distributed across the minibasin and deformation to be focused near the diapir margin resulting in development of stacked halokinetic sequences (Giles and Rowan, 2012; Hearon et al., 2014). Our restorations show that, although primarily controlled by diapir-flank processes, CHS typically present subtle thickness variations (c. 5-15% of their maximum thickness) over a much larger (> 1 km of width) scale (Figs. 8 and 13). The influence of minibasin-scale processes on CHS geometry is variable through time and space. It is typically greater within lower sequences (CHS 1-3 in fig. 5-6; CHSs 1-4 in fig. 10), immediately after the bowl-shaped sequence, which indicates a transitional period in which subsidence and deformation are roughly equally influenced by diapir-margin and minibasin processes. Minibasin-scale subsidence is also more important towards the central portions of linear salt walls where lowermost sequences are controlled by minibasin-scale processes, passing laterally towards their edges into CHSs (CHSs 1-2, figs. 5 and 6, table 3). Ultimately, this demonstrates that diapir-flank and minibasin-scale deformation work in tandem and, in most cases, as a continuum process.

5.5. Implications for hydrocarbon reservoirs

The recognition of km-scale four-dimensional variability of halokinetic and composite halokinetic sequences has implications for the understanding of potential hydrocarbon reservoir distribution within minibasins and the development of diapir-flank stratigraphic (i.e. pinch-out) traps. Reservoir sandstones deposited in channels and lobes will tend to accumulate downdip of diapir-related topographic relief (Matthews et al., 2007; Banham and Mountney, 2013; Hearon et al., 2014). This means that reservoirs will pinch-out updip at or near the axial traces of drape fold developed within CHSs (Fig. 4) (Giles and Rowan, 2012; Hearon et al., 2014). Tabular CHS may, therefore, have reservoir facies in direct contact with the diapir or pinching-out less than 200 m away from it. In contrast, tapered CHS may contain

550 reservoirs that pinch-out 300-1000 m away from the diapir (Fig. 4). As CHSs vary along-strike
551 and across salt walls, reservoir distribution and pinch-out will also vary. The same CHS may
552 have reservoir facies in direct contact with the salt wall on one side and > 300 m away from
553 the diapir on its other side (Fig. 18). Although our work focuses on fluvial-continental and
554 clastic-dominated minibasins, the observed geometric variability of diapir-flank strata can also
555 be applied to shallow- and deep-waters settings influenced by diapirism and, ultimately aid the
556 prediction of reservoir-facies and pinch-out location within minibasins.

557 **6. CONCLUSIONS**

558 This study combines 3D seismic and 2D structural restorations to analyse the interaction
559 between diapirism with minibasin subsidence and deformation, focusing on diapir-flank
560 architecture and development of composite halokinetic sequences. We provide for the first
561 time, a 3D, seismic-based study that evaluates the development of composite halokinetic
562 sequences associated with different geometries and styles of diapirs, demonstrating that
563 CHSs can be highly variable through time and space. We analyse CHS variability within a
564 single minibasins along an inclined salt wall; and within two different minibasins across an
565 upright, broadly vertical salt wall. A single CHS can vary along-strike within the same minibasin
566 and across a diapir. Their large majority (c. 73%) varies laterally across a salt wall, presenting
567 contrasting end-member (i.e. tabular or tapered) geometries. They can also transition into
568 isopachous and broadly undeformed strata away from the diapir or to growth strata associated
569 with salt-related extension or diapir-collapse (i.e. rollovers). These lateral variations can be
570 linked to changes in CHS thickness and/or in the diapir flank geometries. Tabular CHSs are
571 commonly associated with steeper diapir flanks and tapered CHSs with relatively gentler salt-
572 sediment interfaces. CHSs can also be more vertically variable than previously described,
573 presenting more frequent switches in their geometries through the stratigraphic succession or
574 different vertical zonations to the classic CHS models. These are often associated with
575 changes in diapir geometry such as salt shoulders, which are characterized by an abrupt
576 narrowing and gentling of the salt-sediment interface. These features are typically associated

with a marked increase in the width of folding between pre- and post-shoulder CHSs, which can result in the development of different end-member geometries. They can also produce localized downturn and rollover geometries driven by diapir collapse by dissolution.

We explain that these variations are controlled by the three-dimensionally variable length and width of the diapir's roof, which is in turn controlled by a volumetrically variable salt flux and sediment accumulation, as opposed to the two-dimensional A/R ratios from previous works. Ultimately, this study improves the understanding of 3D geometries and variability of diapir-flank strata and associated salt-sediment interface. This may, in turn, aid in the prediction of sedimentary facies and trap geometries within minibasins and contribute to hydrocarbon exploration in diapiric provinces worldwide.

ACKNOWLEDGMENTS

Special thanks to Oliver Duffy and Mark Rowan for discussions. We thank Condor Petroleum for permission to use and publish the seismic data in this study. We also thank Schlumberger for the academic licenses of seismic interpretation software, Petrel©, and Petroleum Experts for 2D Move©, which was used for depth-conversion and structural restorations.

REFERENCES

Banham, S. G., & Mountney, N. P. (2013). Evolution of fluvial systems in salt-walled mini-basins: a review and new insights. *Sedimentary Geology*, *296*, 142-166.

Barde, J. P., Chamberlain, P., Galavazi, M., Harwijanto, J., Marsky, J., Gralla, P., & van den Belt, F. (2002a). Sedimentation during halokinesis: Permo-Triassic reservoirs of the Saigak field, Precaspian basin, Kazakhstan. *Petroleum Geoscience*, *8*(2), 177-187.

Barde, J. P., Gralla, P., Harwijanto, J., & Marsky, J. (2002b). Exploration at the eastern edge of the Precaspian basin: Impact of data integration on Upper Permian and Triassic prospectivity. *AAPG bulletin*, *86*(3), 399-415.

601 Brunet, M. F., Volozh, Y. A., Antipov, M. P., & Lobkovsky, L. I. (1999). The geodynamic
602 evolution of the Precaspian Basin (Kazakhstan) along a north–south
603 section. *Tectonophysics*, *313*(1-2), 85-106.

604 Duffy, O. B., Fernandez, N., Hudec, M. R., Jackson, M. P., Burg, G., Dooley, T. P., & Jackson,
605 C. A. L. (2017). Lateral mobility of minibasins during shortening: insights from the SE
606 Precaspian Basin, Kazakhstan. *Journal of Structural Geology*, *97*, 257-276.

607 Fernandez, N., Duffy, O. B., Hudec, M. R., Jackson, M. P., Burg, G., Jackson, C. A. L., &
608 Dooley, T. P. (2017). The origin of salt-encased sediment packages: observations from the
609 SE Precaspian Basin (Kazakhstan). *Journal of Structural Geology*, *97*, 237-256.

610 Fernandez, N., Hudec, M. R., Jackson, C. A. L., Dooley, T. P., & Duffy, O. B. (2019). The
611 competition for salt and kinematic interactions between minibasins during density-driven
612 subsidence: observations from numerical models. https://doi.org/10.31223/osf.io/jak5u

613 Giles, K. A., Lawton, T. F. (2002). Halokinetic sequence stratigraphy adjacent to the El
614 Papalote diapir, northeastern Mexico. *AAPG bulletin*, *86*(5), 823-840.

615 Giles, K. A., & Rowan, M. G. (2012). Concepts in halokinetic-sequence deformation and
616 stratigraphy. *Geological Society, London, Special Publications*, *363*(1), 7-31.

617 Giles, K. A., Rowan, M.G., Langford, R., McFarland, J., Hearon, T. (2018) Salt Shoulders *in*
618 *AAPG Search and Discovery, AAPG International Conference and Exhibition, London,*
619 *England.*

620 Hearon, T. E., Rowan, M. G., Giles, K. A., & Hart, W. H. (2014). Halokinetic deformation
621 adjacent to the deepwater Auger diapir, Garden Banks 470, northern Gulf of Mexico: Testing
622 the applicability of an outcrop-based model using subsurface data. *Interpretation*, *2*(4), SM57-
623 SM76.

624 Hudec, M. R., & Jackson, M. P. (2007). Terra infirma: Understanding salt tectonics. *Earth-*
625 *Science Reviews*, *82*(1-2), 1-28.

626 Jackson, M. P. A., & Talbot, C. J. (1991). *A glossary of salt tectonics*. Bureau of Economic
627 Geology, University of Texas at Austin.

628 Jackson, M. P., & Hudec, M. R. (2017). *Salt tectonics: Principles and practice*. Cambridge
629 University Press.

630 Jackson, C. A. L., Duffy, O. B., Fernandez, N., Dooley, T. P., Hudec, M. R., Jackson, M. P., &
631 Burg, G. (2019). The Stratigraphic Record of Minibasin Subsidence, Precaspian Basin,
632 Kazakhstan. *Basin Research*.

633 Kergaravat, C., Ribes, C., Legeay, E., Callot, J. P., Kavak, K. S., & Ringenbach, J. C. (2016).
634 Minibasins and salt canopy in foreland fold-and-thrust belts: The central Sivas Basin,
635 Turkey. *Tectonics*, *35*(6), 1342-1366.

636 Martín-Martín, J. D., Vergés, J., Saura, E., Moragas, M., Messager, G., Baqués, V., Razin, P.,
637 Grélaud, C., Malaval, M., Joussiame, R., Casciello, E., Cruz-Orosa, I., Hunt, D. W. (2017).
638 Diapiric growth within an Early Jurassic rift basin: the Tazoult salt wall (central High Atlas,
639 Morocco). *Tectonics*, *36*(1), 2-32.

640 Matthews, W. J., Hampson, G. J., Trudgill, B. D., & Underhill, J. R. (2007). Controls on
641 fluviolacustrine reservoir distribution and architecture in passive salt-diapir provinces: Insights
642 from outcrop analogs. *AAPG bulletin*, *91*(10), 1367-1403.

643 Moragas, M., Vergés, J., Saura, E., Martín-Martín, J. D., Messager, G., Merino-Tomé, Ó., ...
644 & Joussiaume, R. (2018). Jurassic rifting to post-rift subsidence analysis in the Central High
645 Atlas and its relation to salt diapirism. Basin Research, 30, 336-362.

646 Nelson, T. H. (1989). Style of salt diapirs as a function of the stage of evolution and the nature
647 of the encasing sediments. In *Gulf Coast Section SEPM Foundation 10th Annual Research*
648 *Conference Program and Abstracts* (pp. 109-110).

649 Rowan, M. G., & Weimer, P. (1998). Salt-sediment interaction, northern Green Canyon and
650 Ewing bank (offshore Louisiana), northern Gulf of Mexico. *AAPG bulletin*, *82*(5), 1055-1082.

651 Rowan, M. G., Lawton, T. F., Giles, K. A., & Ratliff, R. A. (2003). Near-salt deformation in La
652 Popa basin, Mexico, and the northern Gulf of Mexico: A general model for passive
653 diapirism. *AAPG bulletin*, *87*(5), 733-756.

654 Rowan, M. G., Giles, K. A., Hearon IV, T. E., & Fiduk, J. C. (2016). Megaflaps adjacent to salt
655 diapirs. *AAPG Bulletin*, *100*(11), 1723-1747.

656 Rowan, M. G., & Ratliff, R. A. (2012). Cross-section restoration of salt-related deformation:
657 Best practices and potential pitfalls. *Journal of Structural Geology*, *41*, 24-37.

658 Saura, E., Vergés, J., Martín-Martín, J. D., Messager, G., Moragas, M., Razin, P., ... & Hunt,
659 D. W. (2014). Syn-to post-rift diapirism and minibasins of the Central High Atlas (Morocco):
660 the changing face of a mountain belt. *Journal of the Geological Society*, *171*(1), 97-105.

661 Sclater, J. G., & Christie, P. A. (1980). Continental stretching: An explanation of the post-Mid-
662 Cretaceous subsidence of the central North Sea Basin. *Journal of Geophysical Research:*
663 *Solid Earth*, *85*(B7), 3711-3739.

664 Volozh, Y. A., Antipov, M. P., Brunet, M. F., Garagash, I. A., Lobkovskii, L. I., & Cadet, J. P.
665 (2003). Pre-Mesozoic geodynamics of the Precaspian basin (Kazakhstan). *Sedimentary*
666 *Geology*, *156*(1-4), 35-58.

667 Vendeville, B. C., & Jackson, M. P. (1992). The rise of diapirs during thin-skinned
668 extension. *Marine and Petroleum Geology*, *9*(4), 331-354.

669 ***FIGURES***

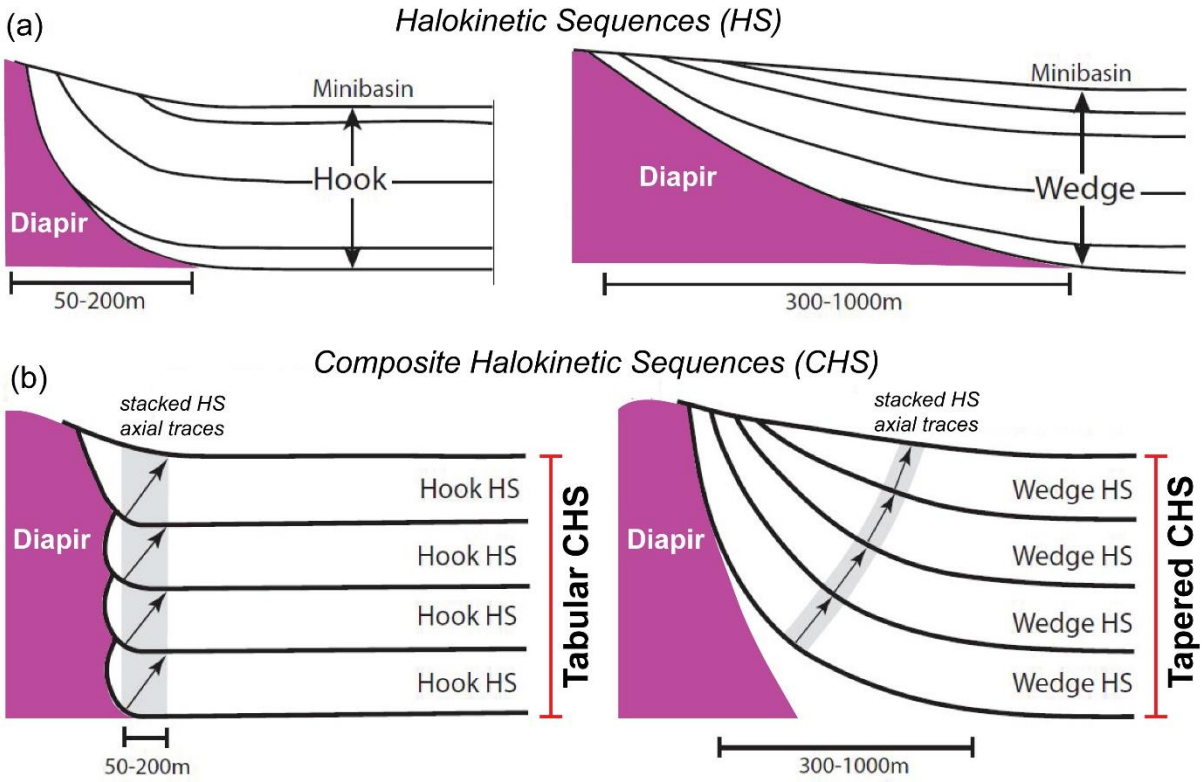

670

671 *Figure 1: (a) End-members of halokinetic sequences (HS), hooks and wedges. (b) End-members of*

672 *composite halokinetic sequences (CHS), tabular and tapered. Adapted from Giles and Rowan (2012).*

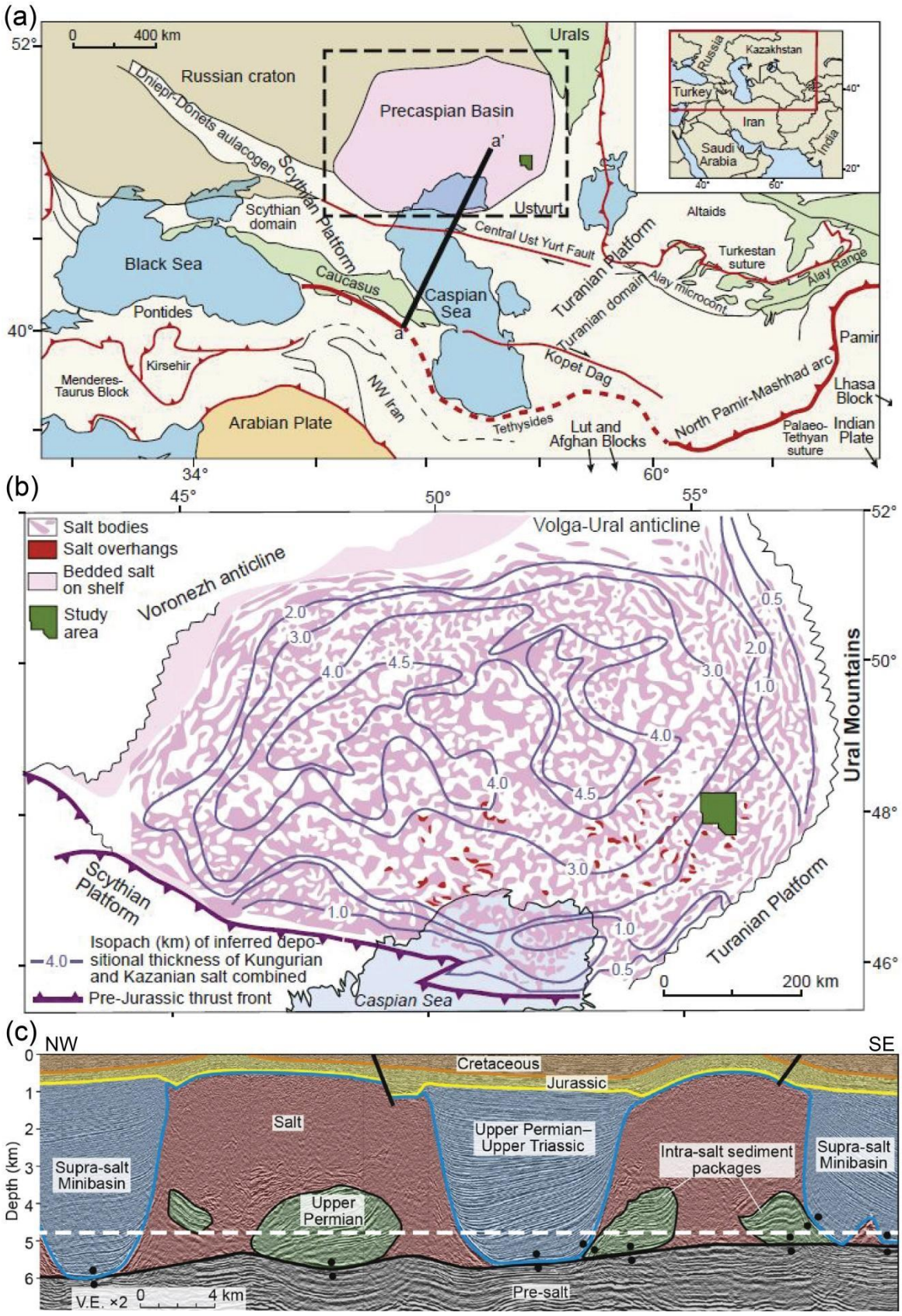

Figure 2 – (a) Regional geological map showing the location and geodynamic context of the Precaspian salt basin (pink). Orogenic belts in green and area in (b) indicated by black dashed lines. (from Duffy et al., 2017 and after Natal'in and Sengor, 2005). (b) Composite salt thickness and structure map adapted

677 from Volozh et al (2003a) and Duffy et al (2017) showing the location of the 3D survey utilized in this
678 study. (c) Composite seismic section illustrating the main salt tectonic structural elements in the study-
679 area, e.g. large salt walls, encased minibasins and Upper Permian-Upper Triassic supra-salt
680 minibasins, the focus of this study (adapted from Duffy et al., 2017).

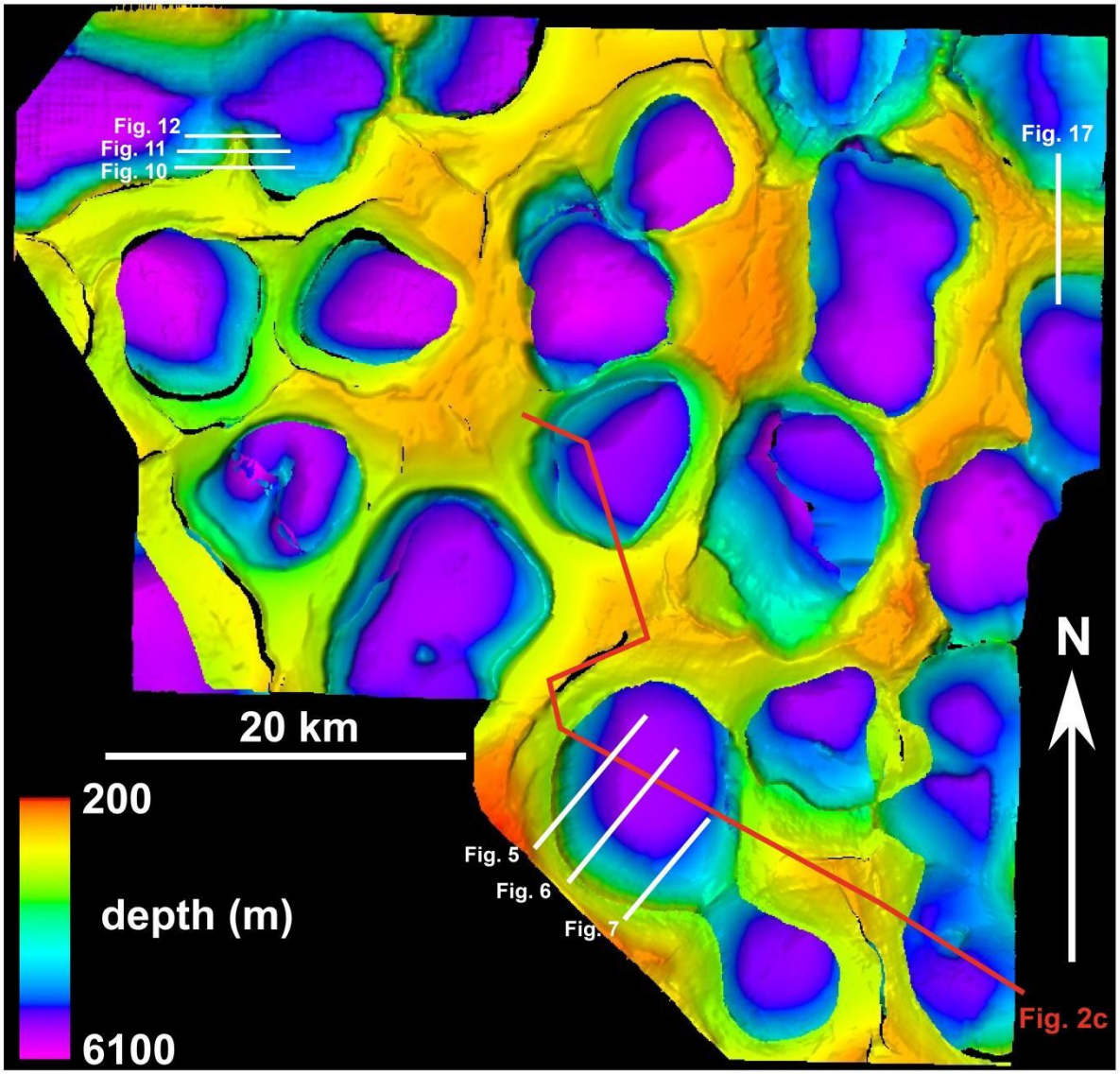

681

682 *Figure 3: Top Salt Depth-Map illustrating the polygonal structural framework of salt walls and elliptical*
683 *to sub-circular minibasins in the study-area. The seismic sections presented in this study are indicated*
684 *in white and another composite section from Duffy et al. (2017) in red.*

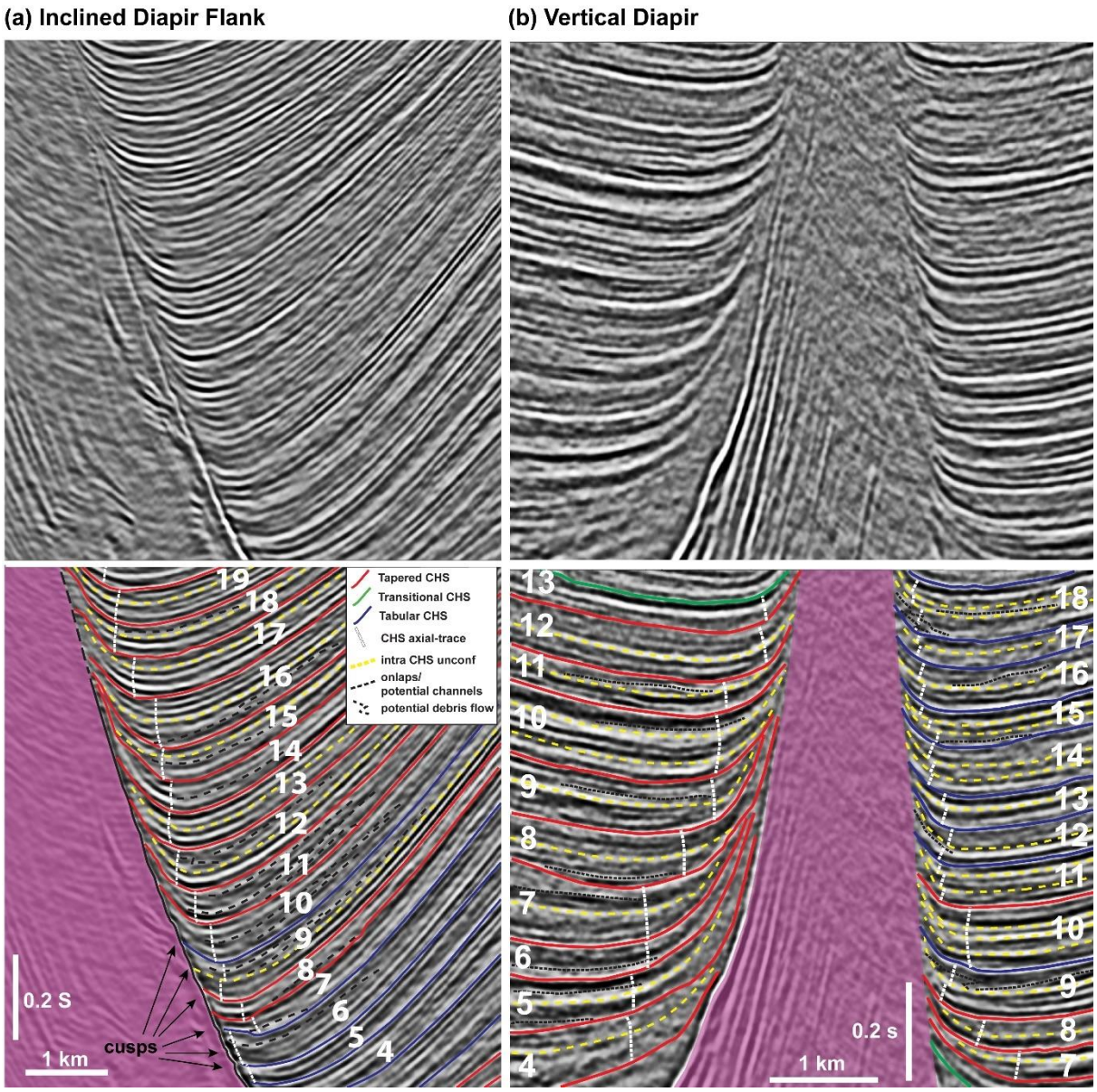

685

686 *Figure 4: Uninterpreted and Interpreted sections showing CHS variability and detailed stratal*
687 *architecture across two distinct diapir-flank geometries: (a) inclined diapir flank and (b) vertical diapir.*
688 *Intra-CHS* unconformities (yellow dashed lines) relate to 4th order Halokinetic Sequences. Basal onlaps
689 and stratigraphic terminations are indicated in black dashed lines and may potentially indicate channels
690 and debris-flow deposits at/near the depositional axis of CHSs.

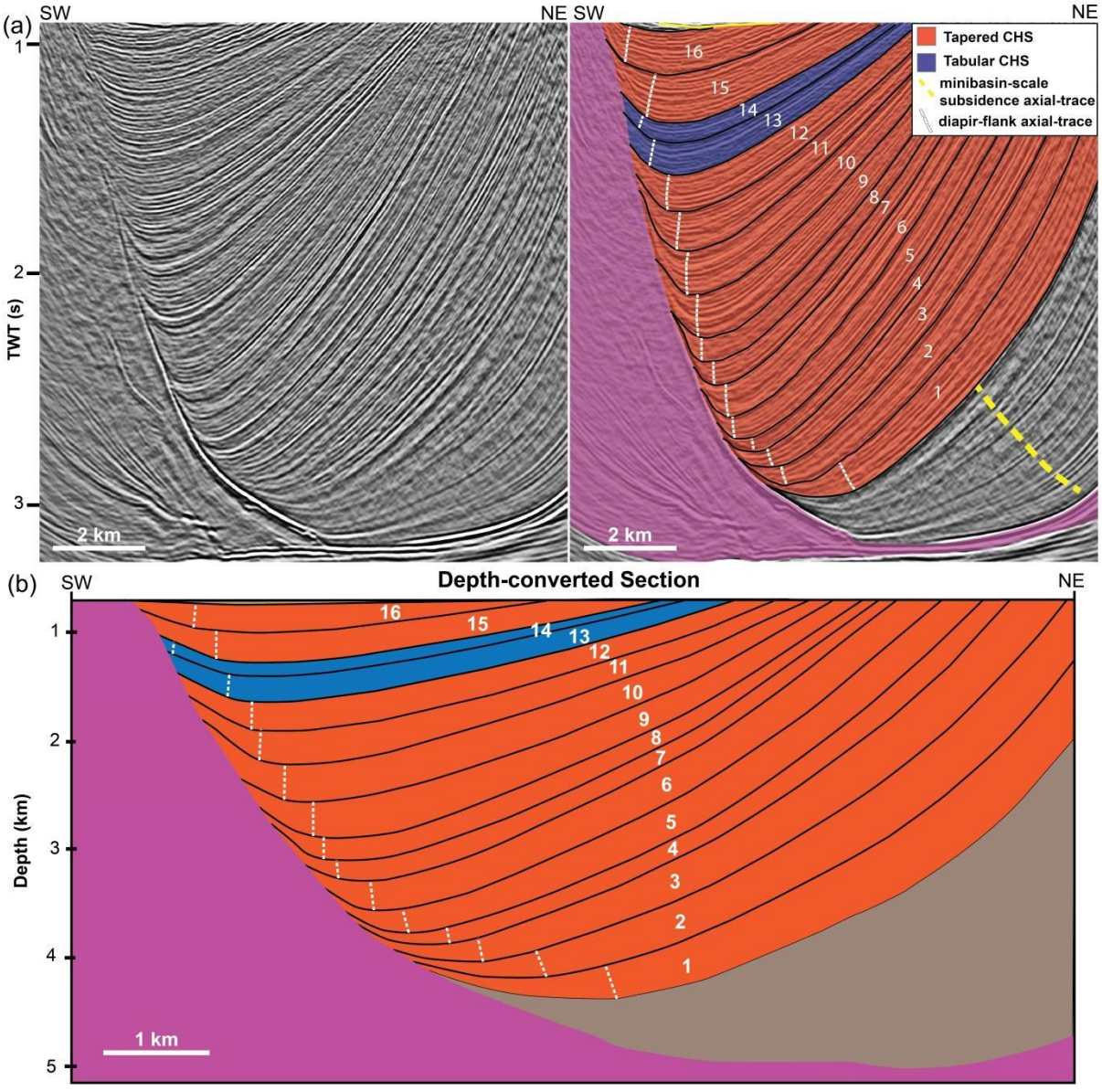

691

692 *Figure 5: (a) Uninterpreted and interpreted seismic profiles of Section 1 illustrating minibasin and CHS*
693 *architecture in the northern portion of the inclined salt wall. (c) Depth-converted section. Minibasin strata*
694 *are tilted to the southwest due to shortening and uplift of a salt wall to the northeast of the section. The*
695 *lowermost minibasin section (brown) is characterized by a broad, bowl-shape geometry indicating*
696 *minibasin-scale, broadly symmetric subsidence. This section is overlain by a large-scale wedge*
697 *sequence composed of a series of CHSs dominated by tapered geometries, i.e. only two tabular CHSs.*

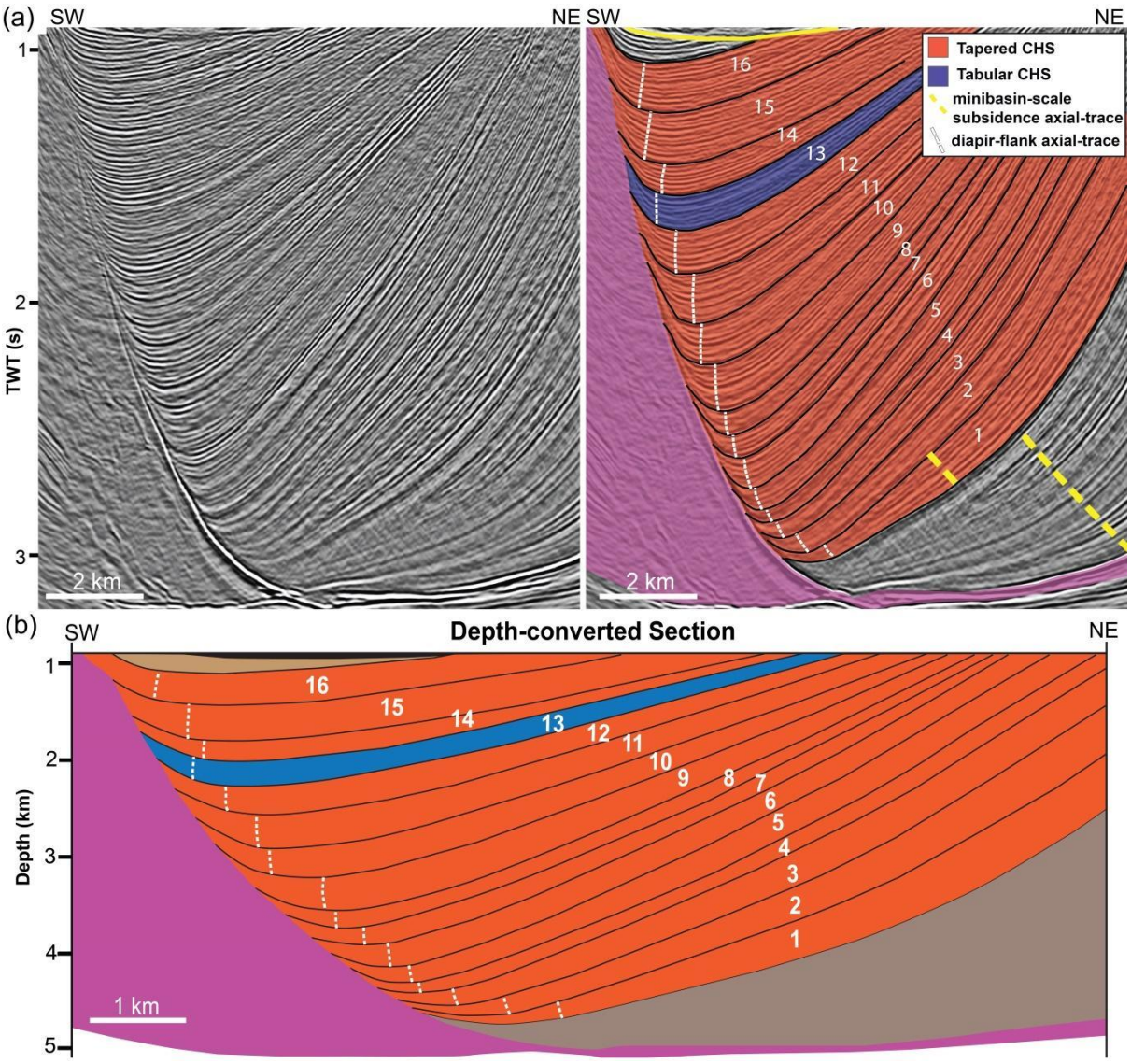

Figure 6: (a) Uninterpreted and interpreted seismic profiles of Section 2 illustrating minibasin and CHS architecture in the central portion of the inclined salt wall. (c) Depth-converted section. Minibasin strata are tilted to the southwest due to shortening and uplift of a salt wall to the northeast of the section. The lowermost minibasin section (brown) is characterized by a broad, bowl-shape geometry indicating minibasin-scale subsidence. This section is overlain by a large-scale wedge succession composed of a series of CHSs dominated by tapered geometries with only one tabular CHS.

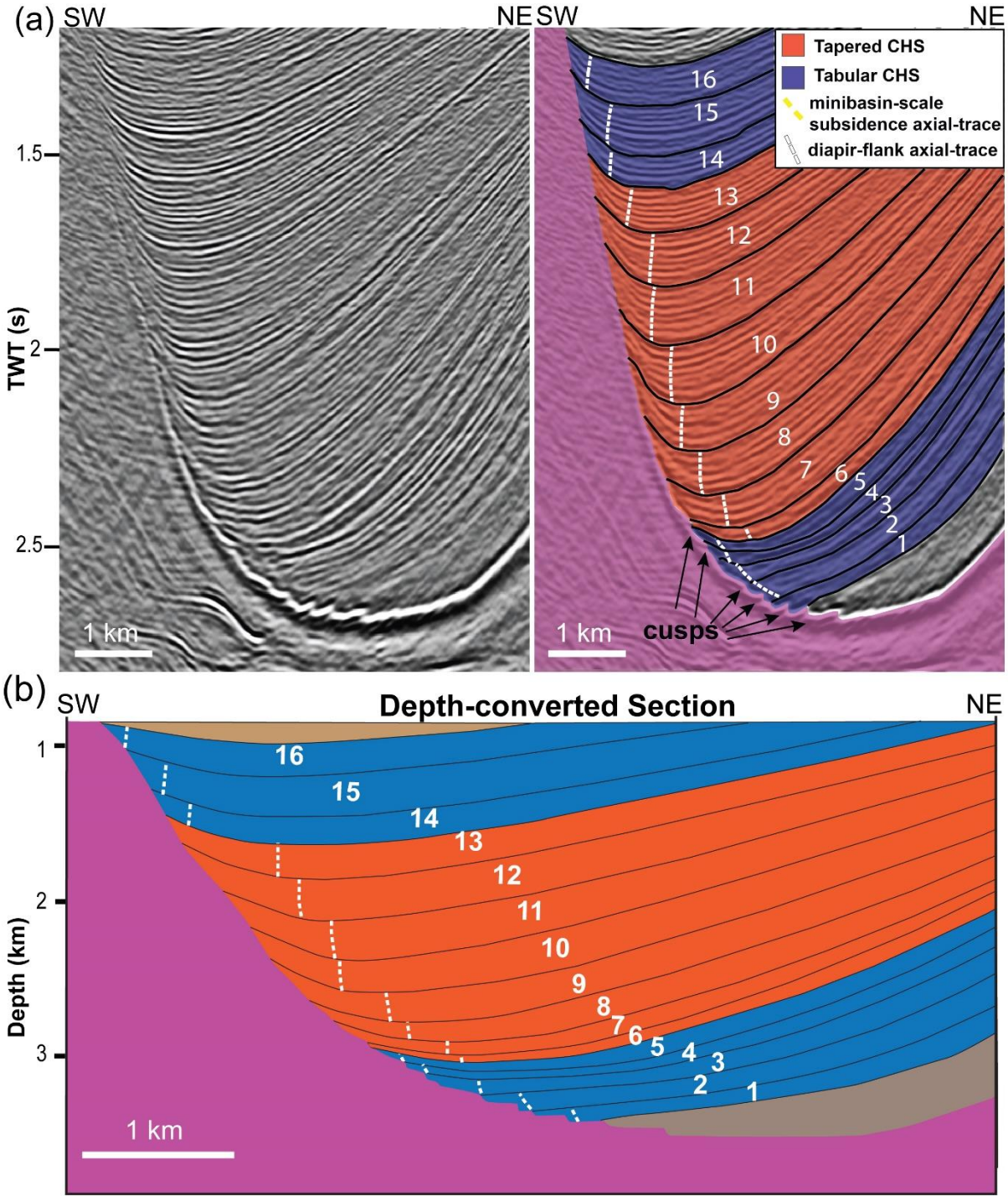

705

706 *Figure 7: (a) Uninterpreted and interpreted seismic profiles of Section 3 illustrating minibasin and CHS*
707 *architecture in the northern portion of the inclined salt wall. (c) Depth-converted section. Minibasin strata*
708 *are tilted to the southwest due to shortening and uplift of a salt wall to the northeast of the section.*
709 *Lower and uppermost undifferentiated sequences in brown and CHSs in blue and red according to their*
710 *end-member geometries. The succession shows an equal proportion of tabular (blue) and tapered (red)*
711 *end-members and an atypical vertical zonation characterized by lower and upper tabular CHSs and*

intermediate tapered CHSs. Prominent cusps occur where bounding unconformities of lowermost CHSs intersect the salt-sediment interface.

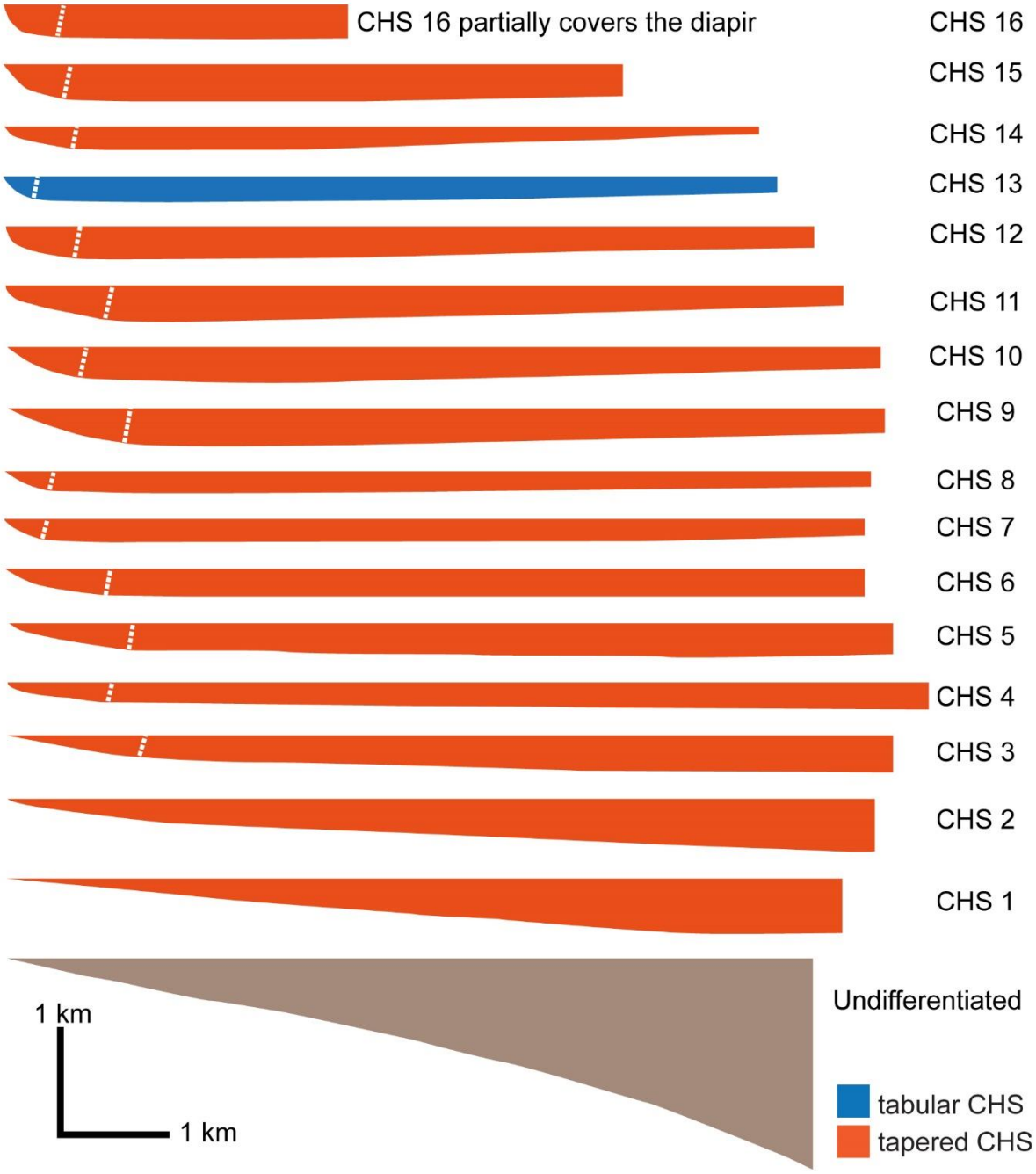

Figure 8: Central section (Section 2) analysis demonstrating the restored geometry and classification for each CHS identified. Dashed white lines represent the restored depositional axial traces associated with monoclinal drape folding characteristic of the CHS development. In many of them, especially oldest CHSs, the influence of broader-scale minibasin subsidence produce very subtle, low-amplitude and high wavelength stratal thinning, which hinders the definition of CHSs 1-2 axial trace.

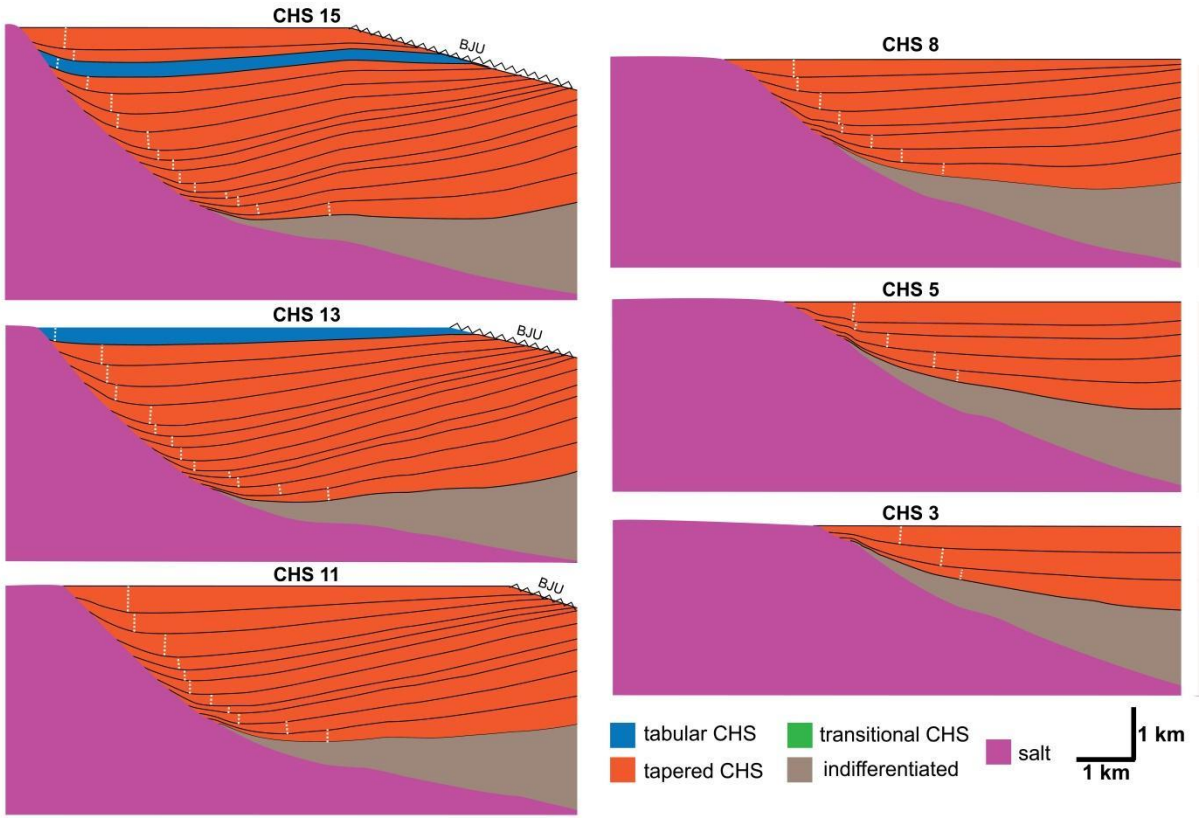

720

721 *Figure 9: Sequential restoration of the central section (Section 2) showing the main, most representative*
722 *steps of minibasin subsidence, development of CHS and their relationship with changes in diapir-flank*
723 *geometries associated with the inclined salt wall. BJU is the Base-Jurassic Unconformity. The white-*
724 *dashed lines represent restored CHS axial-traces.*

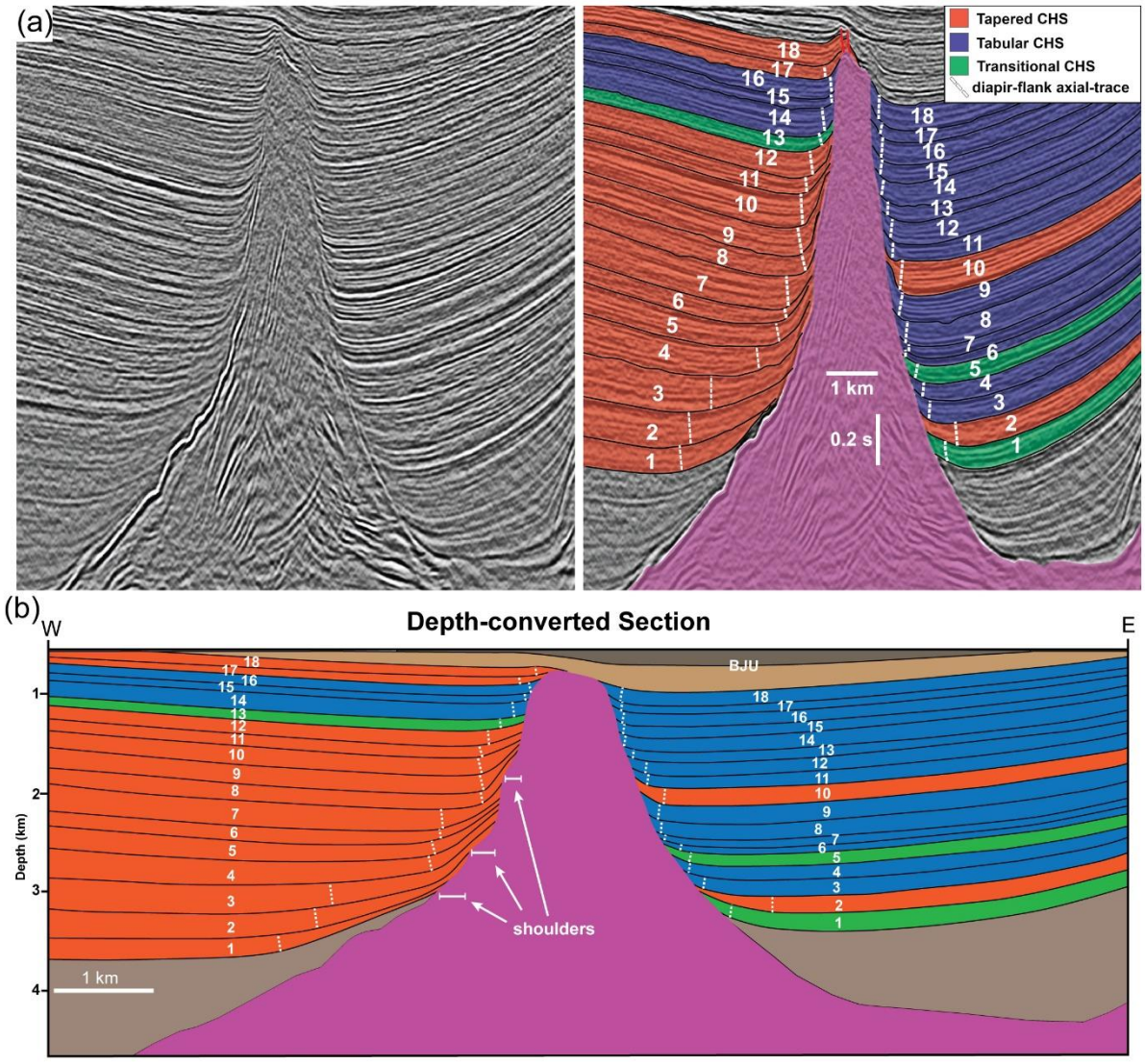

Figure 10: (a) Uninterpreted and interpreted seismic profiles of Section 1 illustrating minibasin and CHS architecture and variability along the southern portion of the vertical salt wall. (b) Depth-converted section. These sections show how the large majority of CHSs change laterally to different CHS end-members along-strike and around the vertical diapir. The western minibasin is dominated by tapered end-members whereas the eastern by tabular end-members. The lowermost minibasin section (brown) is characterized by a broad, bowl-shape geometry indicating minibasin-scale, broadly symmetric subsidence. Uppermost section (light brown) is undifferentiated as it partially covers the diapir and do not present CHSs. BJU is Base-Jurassic Unconformity.

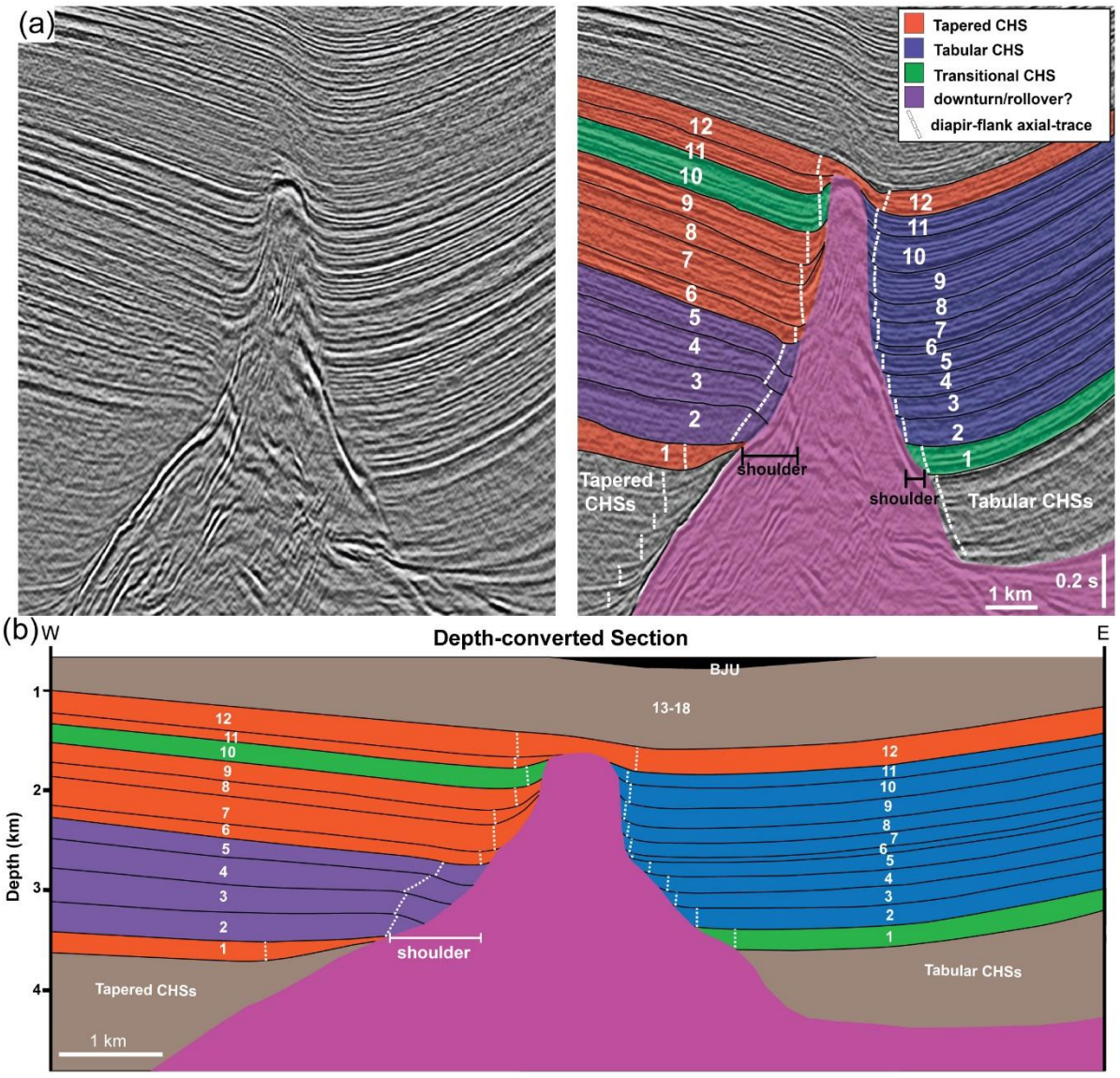

Figure 11: (a) Uninterpreted and interpreted seismic profiles of Section 2 illustrating minibasin and CHS architecture and variability along the central portion of the vertical salt wall. (b) Depth-converted section. Illustrating drastic variability of CHS style across the vertical salt wall, with the eastern minibasin dominated by tabular CHSs and the western minibasin by tapered CHSs. The eastern minibasin presents intermediate sequences with rollover geometries characterized by downturning and thickening towards the diapir above a salt shoulder. The lowermost minibasin section is not numbered but is characterized by tabular CHSs geometries to the east and tapered geometries to the west. The upper section (light brown) is equivalent to the CHSs 13-18 from further south (section 1) but, here, as they cover the diapir, they are not classified as CHSs and, thus, are undifferentiated. BJU is Base-Jurassic Unconformity.

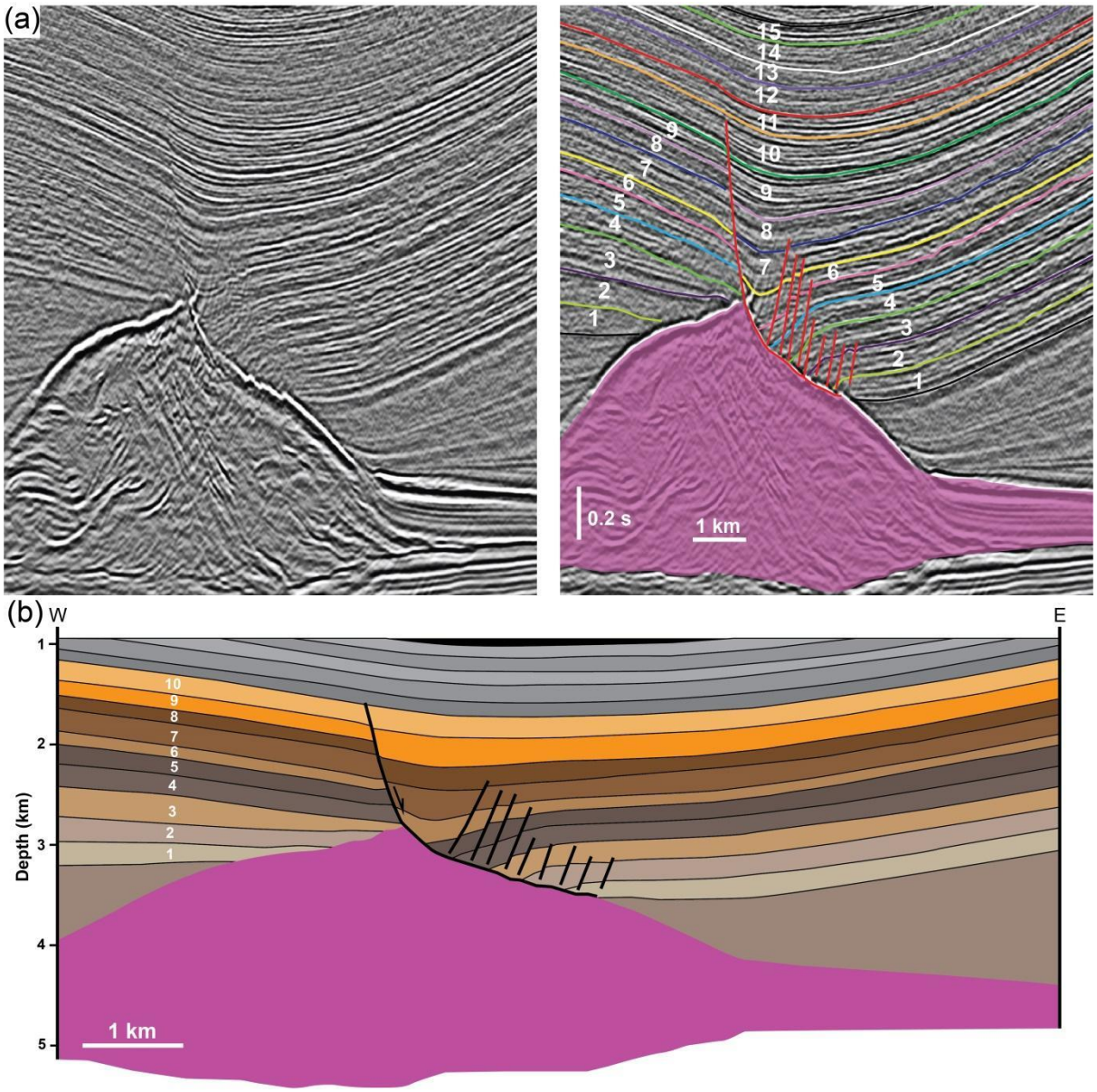

Figure 12: (a) Uninterpreted and interpreted seismic profiles of Section 3, and (b) depth-converted section showing how the salt wall changes to the north to a low-relief salt roller defined by a listric normal fault and a west-dipping extensional rollover. Sequences 1-10 (warm colours) demonstrate rollover and/or hanging-wall thickening geometries denoting syn-extension deposition. Strata equivalent to CHSs further south are no longer classified as CHSs as they are controlled and deformed by the listric normal fault, not being associated with passive diapirism.

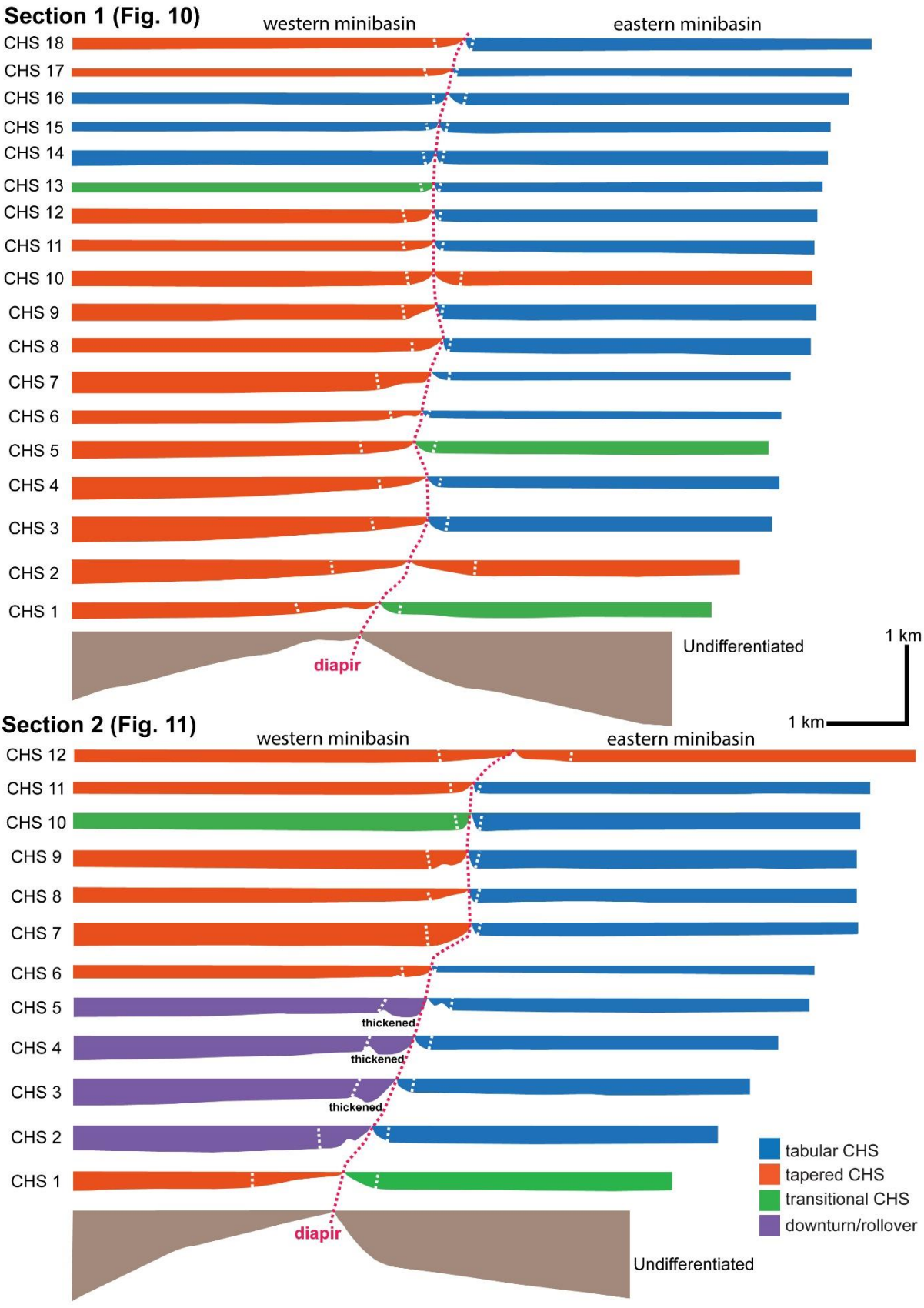

Figure 13: Section analysis for (a) Section 1 (south) and (b) Section 2 (central) demonstrating the restored geometry and classification for each CHS on both western and eastern minibasins around the

vertical diapir. Dashed white lines represent the restored depositional axial traces associated with monoclinal drape folding characteristic of the CHS development. The pink-dashed line indicates the diapir-margin limit of each individual CHS.

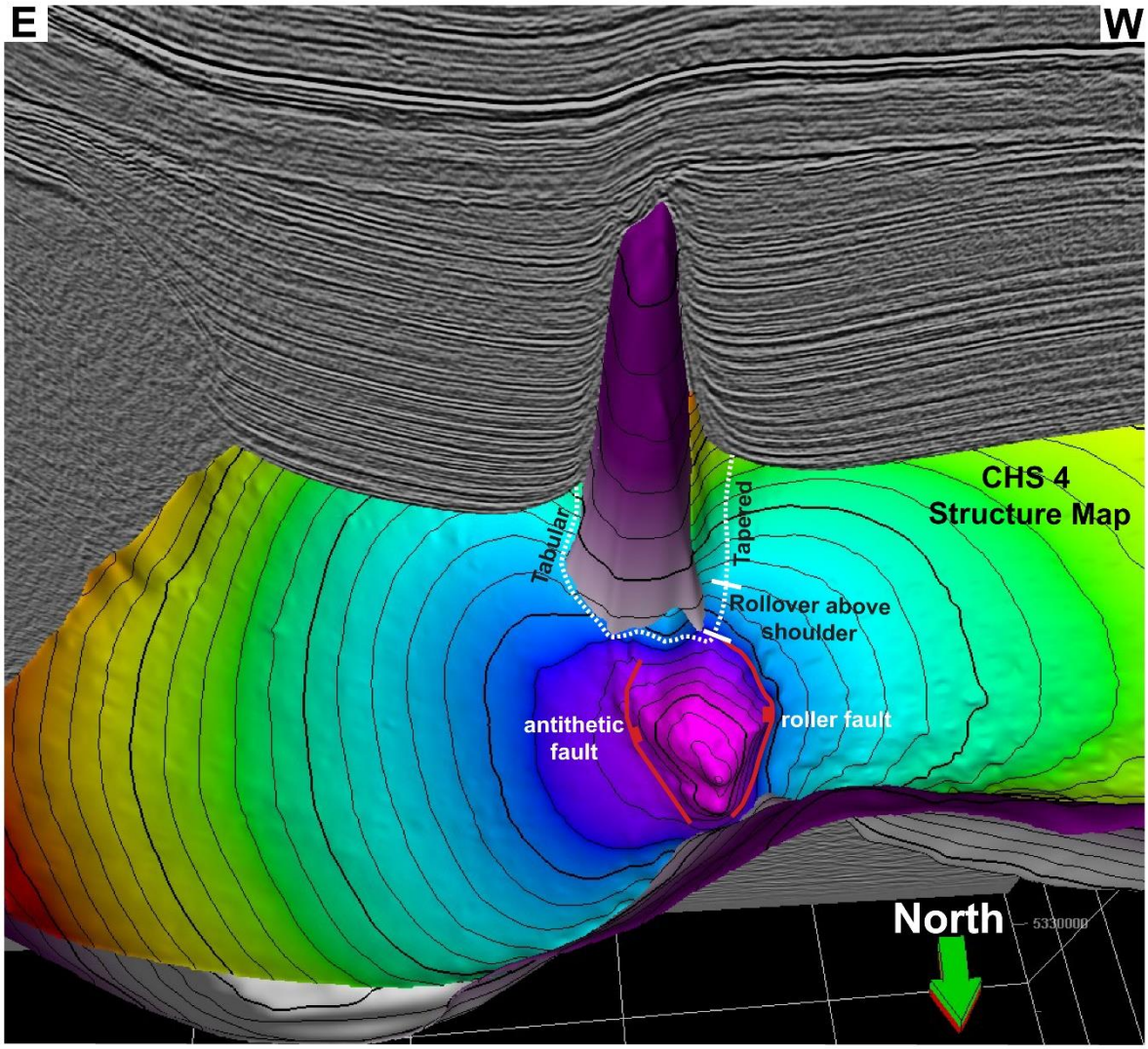

Figure 14: 3D view of the vertical salt wall combined to the CHS 4 structure map demonstrating how CHS architecture changes along-strike and around the wall from tabular CHS geometries to the east and north of the wall to an intermediate rollover above a salt shoulder to the northwest and to tapered CHS geometries to the east. Away from the vertical salt wall, CHS 4 is affected by listric normal faults associated with a salt roller.

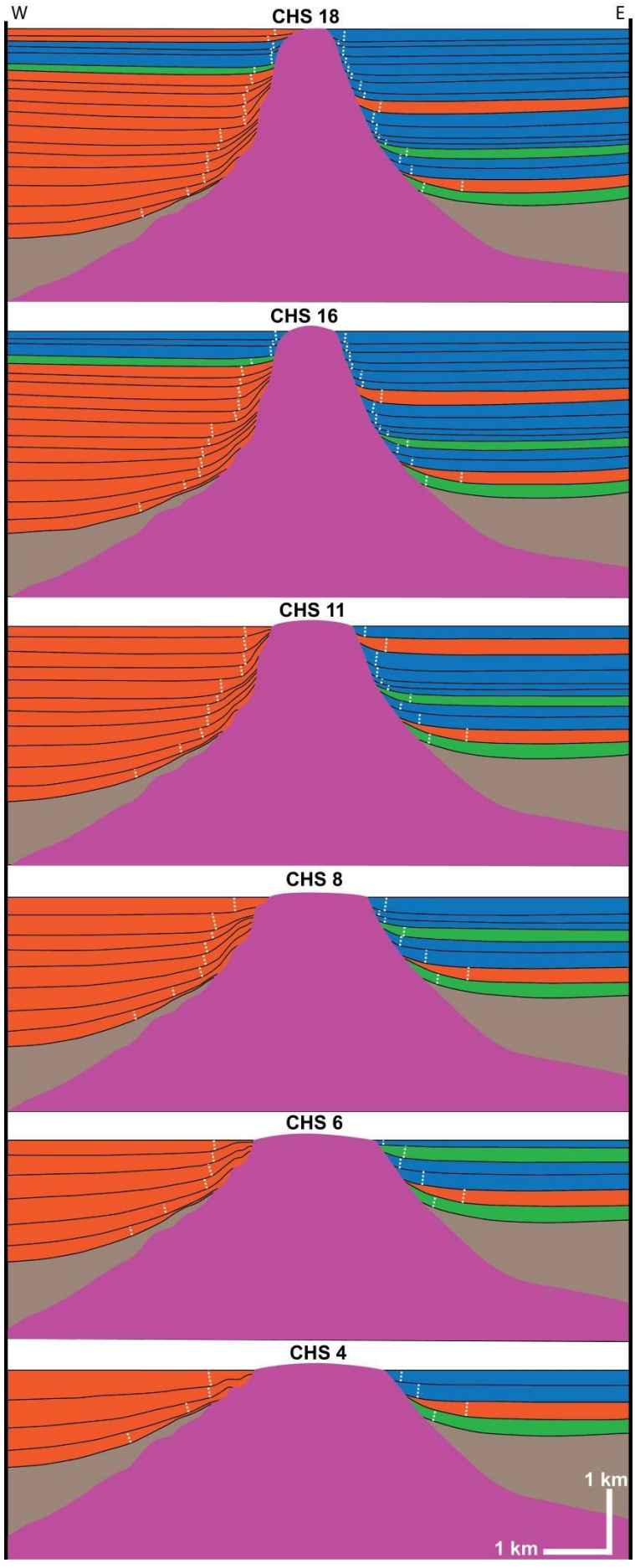

765

Figure 15: Sequential restoration of the southern section (Section 1, figure 10) of the vertical salt wall showing the most representative steps of development of CHS and their relationship with changes in diapir geometries. BJU is Base-Jurassic Unconformity. The white-dashed lines represent restored CHS axial-traces. For the colour classification scheme and figure caption, see figure 9 and 16.

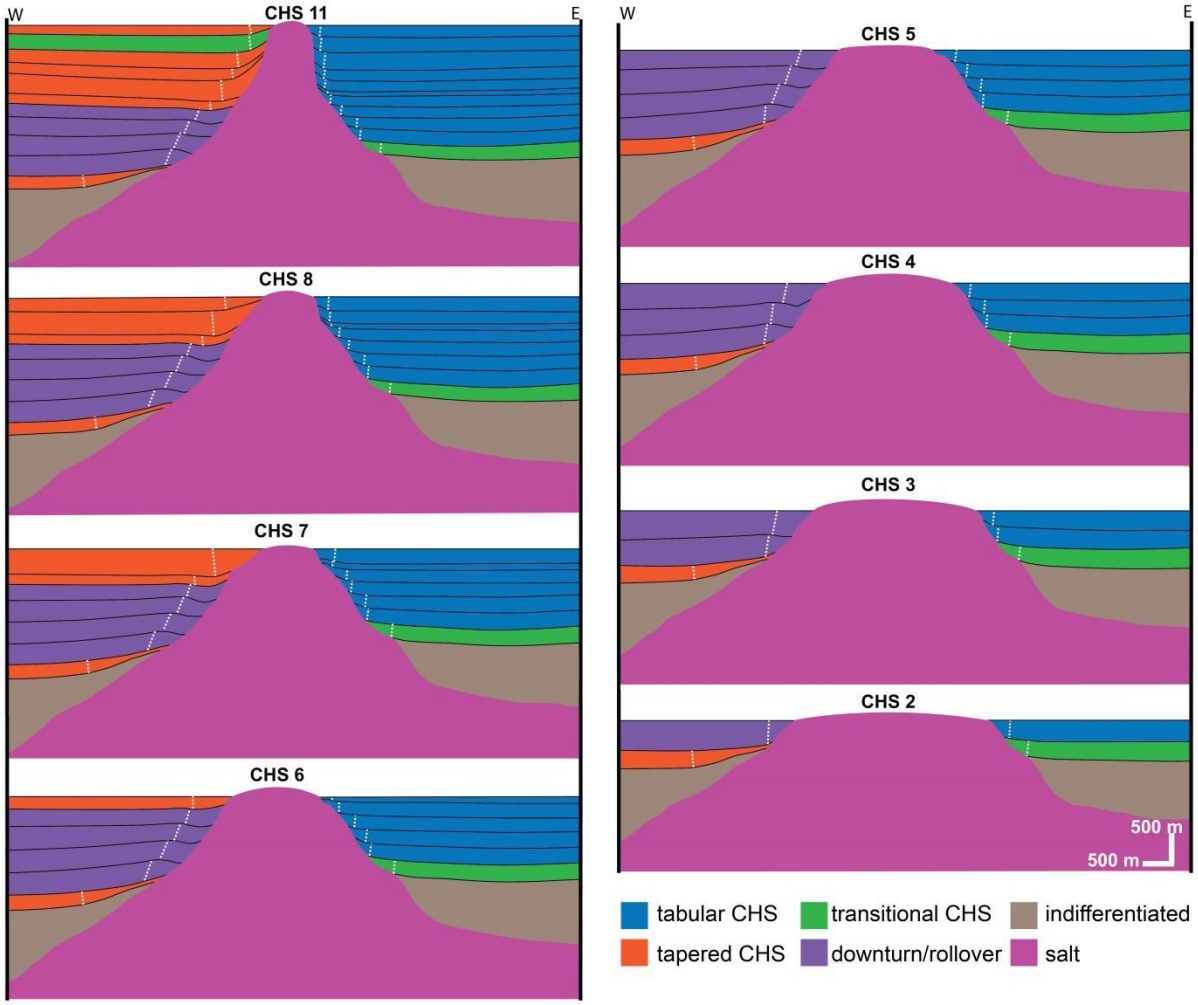

Figure 16: Sequential restoration of the central section (Section 2, figure 11) of the vertical salt wall showing the most representative steps of development of CHS and their relationship with diapir geometries. BJU is Base-Jurassic Unconformity. The white-dashed lines represent restored CHS axial-traces.

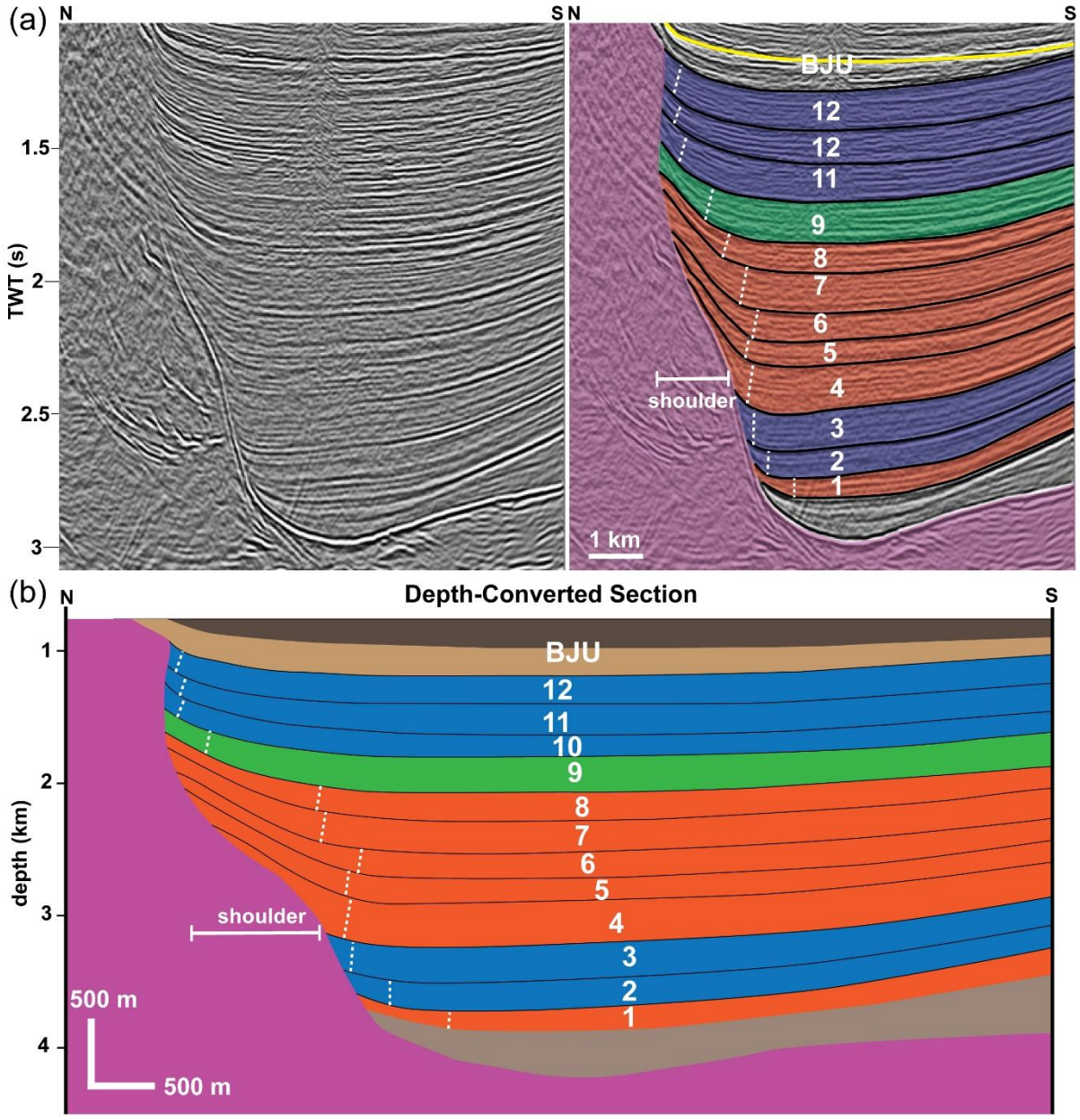

775

776 *Figure 17: (a) uninterpreted and interpreted seismic sections illustrating a CHS succession from a*
777 *different minibasin in the north of the study-area and the transition from pre-shoulder tabular CHSs to*
778 *tapered geometries with significantly wider (c. 500 m) zone of folding and stratal thinning over the*
779 *shoulder. White dashed lines indicate CHS axial-trace. (c) Depth-converted section. Yellow line*
780 *indicates the BJU, Base-Jurassic Unconformity. For colour scheme and classification, see figures 10*
781 *and 16.*

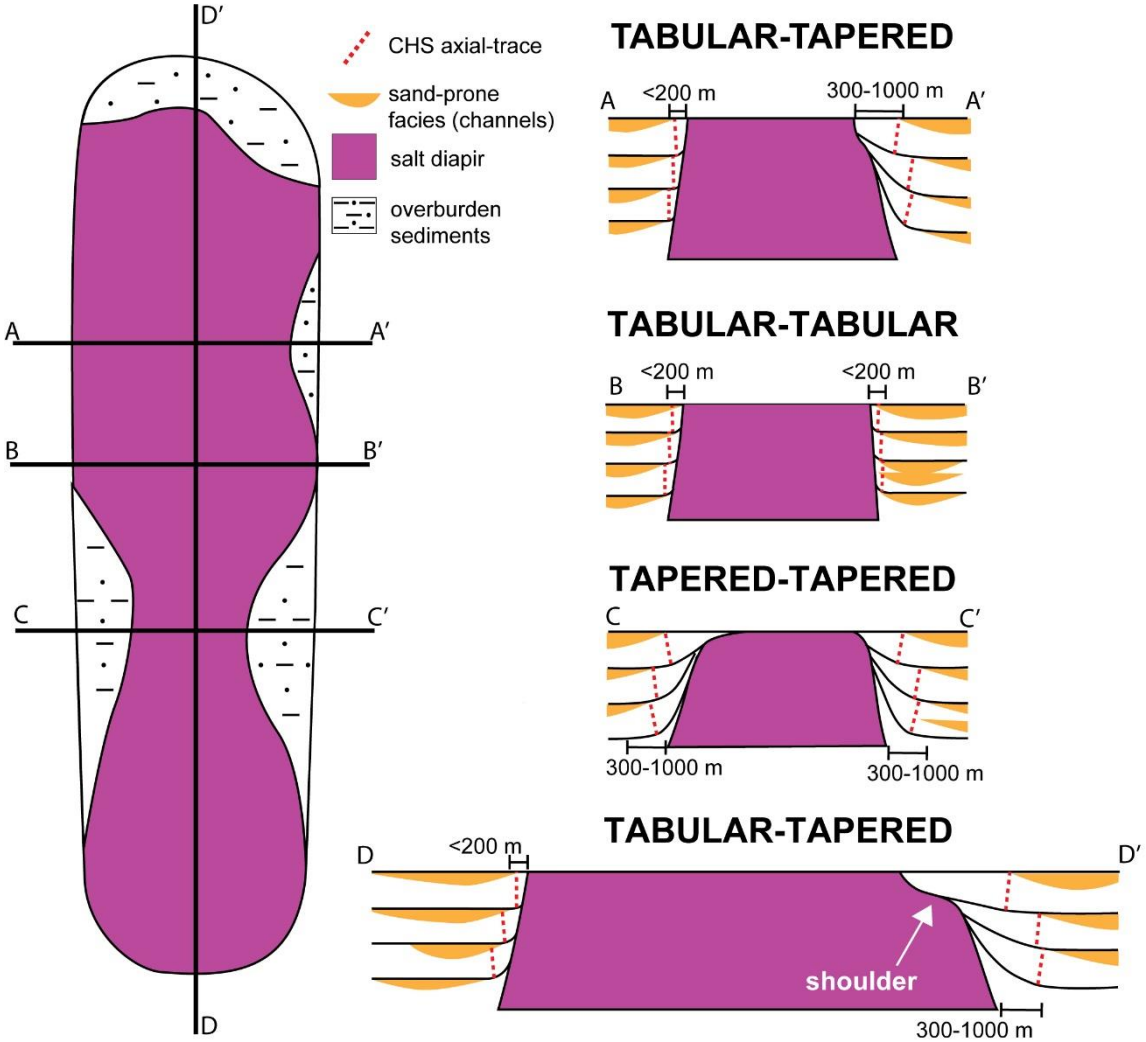

782

783 *Figure 18: Diagram summarizing how diapir-flank and CHS geometries can vary three-dimensionally*
784 *and how this is influenced by how further inboard the cover the diapir, which is turn a consequence of*
785 *volumetrically variable salt flux and sediment accumulation rate. They present variable geometries and,*
786 *in cases, contrasting end-members along a single diapir. This may result in laterally variable distribution*
787 *of sand-prone facies in clastic-dominated systems and, ultimately on diapir-flank reservoir pinch-out.*
788 *Tabular geometries will have updip pinch-outs located up to 200 m from the salt-sediment interface*
789 *whereas in tapered geometries this distance will range from 300-1000 m.*

790

791

792

793

794

TABLES

Inclined Wall												
Section 1 (Northern)				Section 2 (Central)						Section 3 (Southern)			
	Depth-Converted				Depth-Converted		Restored				Depth-Converted		
	Taper Angle	Width of Thinning/Folding zone (m)	CHS type		Taper Angle	Width of Thinning/Folding zone	Taper Angle	Width of Thinning/Folding zone (m)	CHS type		Taper Angle	Width of Thinning/Folding zone (m)	CHS type
CHS16	-	-	Tapered	CHS16	-	-	22	540	Tapered	CHS16	-	-	Tapered
CHS15	30	690	Tapered	CHS15	45	390	32	450	Tapered	CHS15	40	390	Tapered
CHS14	64	90	Tabular	CHS14	33	550	19	630	Tapered	CHS14	60	100	Tabular
CHS13	62	130	Tabular	CHS13	60	170	54	190	Tabular	CHS13	34	470	Tapered
CHS12	32	750	Tapered	CHS12	38	580	23	770	Tapered	CHS12	44	360	Tapered
CHS11	34	750	Tapered	CHS11	33	800	21	950	Tapered	CHS11	33	590	Tapered
CHS10	37	860	Tapered	CHS10	37	690	26	640	Tapered	CHS10	34	560	Tapered
CHS9	30	880	Tapered	CHS9	32	860	22	970	Tapered	CHS9	22	800	Tapered
CHS8	35	645	Tapered	CHS8	26	610	17	690	Tapered	CHS8	12	870	Tapered
CHS 7	31	790	Tapered	CHS 7	16	850	15	950	Tapered	CHS 7	10	930	Tapered
CHS6	28	730	Tapered	CHS6	22	745	20	840	Tapered	CHS6	8	860	Tapered
CHS5	26	900	Tapered	CHS5	18	860	16	980	Tapered	CHS5	8	900	Tapered
CHS4	16	940	Tapered	CHS4	20	640	11	850	Tapered	CHS4	-	140	Tabular
CHS3	13	1250	Tapered	CHS3	11	900	14	975	Tapered	CHS3	-	130	Tabular
CHS2	11	1350	Tapered	CHS2	5	1320	12	1450	MB-scale	CHS2	-	185	Tabular
CHS1	10	2100	MB-scale	CHS1	-	-	7	~ 4500	MB-scale	CHS1	-	175	Tabular

Table 1: Classification and metrics of each CHS mapped in the sections (1-3) for the inclined salt wall. Measurements were obtained from depth-converted sections. For the central section we compare these values for both present-day and restored geometries. The widths of folding were measured from the inflection points to the tips of each CHS and taper angles by straight lines connecting these two points.

Vertical Wall Section 1										
Restored		Restored		CLASSIFICATION			Depth-Converted		Restored	
Taper Angle	Width of Thinning/Folding zone	Taper Angle	Width of Thinning/Folding zone	LEFT MB		RIGHT MB	Taper Angle	Width of Thinning/Folding zone	Taper Angle	Width of Thinning/Folding zone
15	370	13	440	Tapered	CHS18	Tabular	46	190	41	170
12	400	16	460	Tapered	CHS17	Tabular	40	152	36	135
53	150	56	190	Tabular	CHS16	Tabular	71	62	68	75
72	30	72	45	Tabular	CHS15	Tabular	56	83	53	88
62	100	74	50	Tabular	CHS14	Tabular	70	50	60	95
23	280	28	240	Transitional	CHS13	Tabular	65	54	64	60
50	155	52	116	Tabular	CHS12	Tabular	51	118	49	140
18	480	21	430	Tapered	CHS11	Tabular	50	114	46	126
21	350	35	370	Tapered	CHS10	Tapered	26	290	18	310
30	420	49	380	Tapered	CHS9	Tabular	68	105	60	140
22	500	48	420	Tapered	CHS8	Tabular	66	73	61	120
21	850	28	620	Tapered	CHS 7	Tabular	63	45	62	45
20	550	32	550	Tapered	CHS6	Tabular	49	52	40	95
16	790	38	680	Tapered	CHS5	Transitional	33	220	29	270
19	620	38	730	Tapered	CHS4	Tabular	52	120	45	150
14	1070	18	1630	Tapered	CHS3	Tabular	53	130	50	145
13	1100	17	1820	Tapered	CHS2	Tapered	18	810	17	915
11	1180	17	1970	"Tapered"	CHS1	Transitional	44	215	33	270

Table 2: Classification and metrics of the present-day and restored geometries of each CHS mapped in the south section of the vertical salt wall (figure 10). Measurements were obtained from depth-converted sections. The widths of folding were measured from the inflection points to the tips of each CHS and taper angles by straight lines connecting these two points.

Vertical Wall Section 2						
		CLASSIFICATION			Depth-Converted	
Taper Angle	Width of Thinning/Folding zone	LEFT MB		RIGHT MB	Taper Angle	Width of Thinning/Folding zone
-	-	-	CHS18	-	-	-
-	-	-	CHS17	-	-	-
-	-	-	CHS16	-	-	-
-	-	-	CHS15	-	-	-
-	-	-	CHS14	-	-	-
-	-	-	CHS13	-	-	-
-	470	Tapered	CHS12	Tapered	-	340
21	325	Tapered	CHS11	Tabular	67	87
38	240	Transitional	CHS10	Tabular	86	25
42	350	Tapered	CHS9	Tabular	82	36
33	470	Tapered	CHS8	Tabular	84	20
49	450	Tapered	CHS 7	Tabular	77	45
16	420	"Tapered"	CHS6	Tabular	80	20
-	540	Downturn/RV	CHS5	Tabular	46	200 (transition to shoulder)
-	680	Downturn/RV	CHS4	Tabular	54	130
-	520	Downturn/RV	CHS3	Tabular	53	90
-	370	Downturn/RV	CHS2	Tabular	47	160
11	1100	Tapered	CHS1	Transitional	29	295 (transition to shoulder

Table 3: Classification and metrics of the present-day and restored geometries of each CHS mapped in the central section of the vertical salt wall (figure 11). Measurements were obtained from depth-converted sections. The widths of folding were measured from the inflection points to the tips of each CHS and taper angles by straight lines connecting these two points. CHSs 2-5 present distinct downturned and thickened strata in the western minibasin and, thus, are classified as rollover (RV) sequences. Sequences 13-18, defined as CHS further south (Section 1), are not classified as such here as they cover the diapir and, therefore, do not present typical CHS folding and thinning strata